WADC TECHNICAL REPORT 54-368, PART 1
ASTIA DOCUMENT NUMBER AD-97322

TRANSIENT AERODYNAMICS OF TWO-DIMENSIONAL AIRFOILS

Part 1 - Interferometric Measurements of Two-Dimensional Airflow Development About a Symmetrical Double-Wedge Airfoil in Shock-Initiated Subsonic Flow

J. Ray Ruetenik
Emmett A. Witmer

Massachusetts Institute of Technology

August 1956

Aircraft Laboratory
Contract No. AF 33(038)-8906
Project No. 1350

Wright Air Development Center
Air Research and Development Command
United States Air Force
Wright-Patterson Air Force Base, Ohio

FOREWORD

This report was prepared at the Aeroelastic and Structures Research Laboratory, Massachusetts Institute of Technology, Cambridge, Massachusetts, on Air Force Contract Number AF 33(038)-8906, under Project Number 1350, (U) "Atomic Weapon Effects on Aircraft Systems." The work was administered under the direction of the Structures Branch of the Aircraft Laboratory, Wright Air Development Center, with Mr. Francis J. Janik, Jr., acting as project engineer. This report is one of a series of reports which will appear as parts of WADC TR 54-368, "Transient Aerodynamics of Two-Dimensional Airfoils."

The experimental results obtained herein were obtained through the use of the shock tube facility at MIT, which was designed and constructed under Air Force sponsorship.

The writers desire to express appreciation to Professors R. L. Bisplinghoff and H. G. Stever of the MIT Aeronautical Engineering Department for their direction and advice. Dr. Walter Hermann and Mr. Vaughn L. Beals, Jr. conducted the substantial part of the shock tube tests and aided in a preliminary analysis of the data. Mr. Eugene DiFrancesco lent substantial assistance during the experimental phases of this study. Mr. George A. Reitano is thanked for his careful preparation of the airfoil model used in the experiments. Mr. Alfred Holland, Mr. George Tingus, and the MIT Aeroelastic and Structures Research Laboratory Computing Staff assisted in the data reduction phase of this work. Dr. Norman P. Hobbs is thanked for his contributions and suggestions.

Mssrs. John McHugh, James R. Friery and George Falla prepared the illustrations. Miss Kathryn Roberts and Mrs. B. Marks are thanked for their careful typing of the text.

ABSTRACT

Interferometric measurement of the transient pressure distribution and aerodynamic coefficients on a 10-percent-thick symmetrical double-wedge airfoil in shock-initiated subsonic (M=0.4) flow are presented. These results are compared with several theories for somewhat similar gust-type flows. Since the measurement of airforces on an airfoil in a shock tube is a new technique, a critical examination is made of the shock tube as a testing facility and the optical measuring technique employed; in particular, the steady-state pressure distribution is compared with wind-tunnel measurements and perfect-fluid theory.

PUBLICATION REVIEW

This report has been reviewed and is approved.

FOR THE COMMANDER:

for Carl A. Ruetkut
Daniel D. McKee
Colonel, U.S.A.F.
Chief, Aircraft Laboratory
Directorate of Development

TABLE OF CONTENTS

TABLE OF CONTENTS (cont.)

LIST OF FIGURES

LIST OF FIGURES (Cont'd.)

LIST OF TABLES

LIST OF COMMON SYMBOLS

a	speed of sound
c	airfoil chord
C_{D_p}	pressure-drag coefficient
C_L	lift coefficient
$C_{M_{c/2}}$	moment coefficient about midchord
C_p	local pressure coefficient $\left(\frac{p-p_2}{q_2}\right)$
cp.	x-component of distance of center of pressure from the leading edge
M	Mach number of flow, coordinates fixed on shock tube or wind tunnel
N	interferogram fringe number
p	pressure $p_{21} = p_2/p_1$
q	dynamic pressure $q_2 = \frac{1}{2} \rho_2 u_2^2$ $q = \frac{1}{2} \rho u^2$
R_{e_2}	Reynolds number, based on the length c
s	distance a particle moving at u_2 has moved since t=0
S	distance shock has moved, based on U, since t=o

LIST OF COMMON SYMBOLS (Cont'd.)

t	time, t=0 when shock reaches leading edge of airfoil
Δt_d	time interval between shock passage at the detection station 70 in. ahead of airfoil leading edge and occurrence of spark for interferogram
Δt_s	time interval between shock passage at the detection stations 70 in. and 34 in. ahead at airfoil leading edge
T	air temperature
u	x' - component of particle velocity
U	velocity of the flow-initiating shock
x	chordwise distance from airfoil leading edge
x'	distance from airfoil leading edge parallel to shock-tube axis
α	angle of attack
γ	ratio of specific heats
ρ	air density

LIST OF COMMON SYMBOLS (Cont'd.)

subscripts

1	refers to initial conditions in the expansion chamber
2	refers to conditions directly behind the flow-initiating shock
4	refers to initial conditions in the compression chamber

superscript

$(\tilde{\ })$	refers to flow conditions following passage of the incident shock based on the tentative correction explained in the text

SECTION I

INTRODUCTION

The prediction of the transient development of air forces on lifting surfaces has been of interest for many years. Well known are the analyses by Wagner[1] for a sudden change in angle of attack, and Kussner[2] and Karman and Sears[3] for the penetration of a sharp-edged gust. These are for an incompressible fluid. The compressible case was worked out by Lomax, Heaslet, Fuller, and Sluder,[4] and more recently in a somewhat different method by Mazelsky[5] and by Mazelsky and Drischler.[6] These cases are shown schematically in Fig. 1a and b.

Until the advent of the shock tube, no satisfactory method has been available to subject a model to a step-function type of flow field. But as often happens the problems that can be set up in the laboratory are not those that are readily amenable to analytic solution. The "step" in the shock tube, Fig. 1c, consists of a step in the velocity (normal to the shock front) as well as the pressure, density and temperature, whereas the classical sharp-edged gust, Fig. 1b, is a step in the (vertical) velocity only. During the period of shock passage over the airfoil the pressure step is not to be neglected: the direct contribution of the discontinuity in the pressure field to the lift and drag as it sweeps over the airfoil is appreciable. Furthermore, the classical gust front is fixed in space, in contrast to a shock or blast front. In an unpublished work by Hobbs[7] the incompressible sharp-edged gust front is permitted to sweep at an arbitrary speed forward or rearward over the airfoil, Fig. 1d. It is hoped that the unreality of the sudden acquisition of the gust velocity by the particles at the gust front is outweighed by the similarity of the motion of the gust front to the motion of the shock. Comparison will be made to these

Manuscript released by the authors April 27, 1956 for publication as a WADC Technical Report.

results of gust analyses in an attempt to correlate the shock tube data, but the differences from the analytical models should be kept in mind.

Several analyses have been made for a shock passing over a wall with a bump. Most recent is that by Ting and Ludloff,[8] the passage of a strong shock over, loosely speaking, a "bump" in the wall, or more precisely, over an arbitrary flat surface, Fig. 2a. The interpretation of this problem to the subsonic double-wedge airfoil is shown in Fig. 2b. The upstream stagnation streamline is replaced by the wall, which is straight until the shock reaches the airfoil, and then becomes deformed. Herein lies the difficulty. Since the shape of the stagnation streamline is not known for the subsonic double-wedge airfoil, and in fact is also a function of time, the solution to the present problem remains open.

In the present investigation the development of the air forces on a 10-percent-thick symmetrical double-wedge airfoil subjected to shock-initiated flow has been measured by interferometric means in the M.I.T. 8- by 24-inch shock tube. The Mach number of the flow behind the shock was 0.4, and the angles of attack were 0°, 4°, and 8.3°, the latter being approximately the steady-state stall angle of the airfoil as found in wind-tunnel tests. The Reynolds number was 650,000, except for one series of tests at R_e = 1,230,000 and an airfoil angle of attack of 4°.

This investigation is a portion of a program to determine the transient development of air forces on various aerodynamic bodies in motion and subjected to a blast arriving from an arbitrary direction.

SECTION II

EXPERIMENTAL

2.1 Aerodynamic Facility

The experiment was conducted in the 8x24 in. M.I.T.-W.A.D.C. shock tube which will be fully described in reference 9. An overall view is shown in Fig. 3, and the important dimensions are given in Fig. 4. The diaphram and test sections are shown in Fig. 5 and 6. All tests were conducted using ambient air in both the compression chamber and the expansion chamber, with a pressure ratio across the shock of $P_{21} \equiv P_2/P_1 = 1.79 \pm 0.02$ and a particle Mach number behind the shock of $M_2 = 0.4$. The subscripts 1 and 2 apply to conditions ahead and immediately behind the flow-initiating shock at the test station. In order to vary the Reynolds number two values of p_1 were used, 0.5 and 1 atmosphere. The angle of attack, α , of the airfoil was 0, 4, and 8.3 degrees. The test conditions for each run are tabulated in Table I. The Reynold number, Re_2, is based on the chord, c.

All runs were made with a 10-percent-thick symmetrical double-wedge airfoil machined from steel to a 3.962-in. chord, and hardened. This shape was employed for its ease in computing lift forces, etc. The airfoil was supported by clamping between the windows (see Fig. 7).

2.2 Shock-Initiated Flow

A schematic of the ideal shock-tube flow properties is shown in Fig. 8. The undisturbed flow behind the shock was computed from measurements of p_1, the initial air temperature, T_1, and the shock speed, U. The equations are derived in reference 10, and are presented below

$$\rho_1 = \frac{P_1}{RT_1} \tag{2.1}$$

$$a_1^2 = \gamma_1 RT_1 \tag{2.2}$$

$$u_2 = \frac{P_{21} - 1}{\gamma_1[\beta_1(\alpha_1 P_{21} + 1)]^{1/2}} \; a_1 \tag{2.3}$$

$$\rho_2 = \frac{1 + \alpha_1 P_{21}}{\alpha_1 + P_{21}} \; \rho_1 \tag{2.4}$$

$$T_2 = \left[\frac{P_{21}(\alpha_1 + P_{21})}{1 + \alpha_1 P_{21}}\right] T_1 \tag{2.5}$$

where $\alpha_1 \equiv \frac{\gamma_1+1}{\gamma_1-1}$, $\beta_1 \equiv \frac{\gamma_1-1}{2\gamma_1}$

and a is the speed of sound, u the particle speed, ρ the density, and γ the specific-heat ratio. A value of $\gamma = 1.407$ was taken from Hirschfelder and Curtiss [11] for saturated air at 75°F. and 1 atmosphere pressure (Dry air is 1.409), and R = 1716.4 ft. lb./slug °R. The pressure p_1 was measured by a mercury barometer in combination with either an Alphatron vacuum gage(model 511) or a Heise bourdon gage readable to 1/4 psi. The latter gage was necessary as the shock tube was closed during all the tests. The ambient air temperature was measured, and was assumed to represent the temperature in the expansion chamber of the shock-tube immediately prior to a test firing. At least one minute was allowed for the air in the expansion chamber to reach equilibrium with the shock tube This measurement needs refinement, but is probably satisfactory for the present tests. The shock speed, U, was measured by two Schlieren systems located 70 in. and 34 in. upstream from the airfoil mid-chord position. The passage of the shock deflected the light beam about the knife edge in each Schlieren system, which was de-

tected by a photo-multiplier tube and a pulse was sent to the 1/1,600,000 - second increment Potter Counter Chronograph. A block diagram of the circuit is shown in Fig. 9b. The measured time interval between the two pulses, Δt_s, (see Fig. 9a) was used to compute the shock speed U. This measurement is estimated to be accurate to 0.2 percent, the largest effect being due to a 3 μ - second delay in the amplifier-gate.

These measurements to obtain the shock strength were checked by comparing the density jump of an ideal shock at these conditions (Δt_s, p_1, and T_1) to the density jump across actual shocks at the test station as measured by the white-light fringe (described in reference 12) shift in the interferograms (no model was present). They agreed within one percent. The error in the Δt_s measurement discussed above would account for most of this deviation. The balance may be due to errors involved in the measurement of T_1. Plans are being made to measure T_1 directly, but it is not expected to affect the results significantly. A one-degree Fahrenheit error in T_1 gives a one-percent error in the dynamic pressure behind the shock, q_2. A few remarks will be made below concerning significant deviations in the flow behind the shock from the step function (of ideal shock tube theory) as found from a few exploratory measurements made recently. This is a relatively recent observation in shock-tube work and the magnitude of the deviation from the ideal case is somewhat unexpected and will be discussed below.

2.3 Interferometry and Test Procedure

A Mach - Zehender interferometer, Fig. 10, was employed to measure the density distribution around the airfoil. The system will be described in detail in reference 9. The optics are 7 in. in diameter. An Edgerton, Germeshausen, and Grier spark source with a 1 μ-sec. duration filtered to 4481 Å is the light source. The interferometer optics were adjusted so that

the interferograms were the so-called infinite-fringe type where each fringe is an isopycnic, i.e. it connects points of equal density. Stresses in the windows due to clamping the airfoils induced initial fringe deviations, which reached a maximum at the mid-chord, being up to a 2-fringe correction. This correction was made to the final fringe values, and was the chief source of optical error in measuring the density about the airfoil. It is estimated to be accurate to about 1/4 fringe, or an uncertainty in lift of 5 percent at $\alpha = 4$ deg.

The optics of the interferometer were demonstrated to be very stable during the period of each test. The fringe pattern was observed both over long periods of time under static conditions, and also following firing till long after the duration of an experiment, using a strip-film camera. A minute amount of fringe vibration does come through the supports from building vibration, even with shock mountings, but the fringe movement throughout the field is uniform, and hence the resulting error in density distribution is negligible.

One interferogram was made per firing of the shock tube, each at a successively greater time after the shock passed the leading edge of the airfoil. They are shown in Fig. 11. The time parameter $\frac{s}{c} = \frac{u_2 \Delta t_s}{c}$ will be employed in the presentation of the data. The value of s was determined in two ways (refer to Fig. 9a): (1) Where the shock was visible in the interferogram, S, which is the displacement downstream from the leading edge of the airfoil, was measured from the interferogram and s was computed using the measured shock speed, U, and computed particle-velocity component parallel to the shock-tube axis

$$s = \frac{u_2}{U_s} S$$

and (2) For the other cases a photo-multiplier tube within the

interferometer was arranged to detect the spark, and the pulse was fed into a second 1/1,600,000-second increment Potter Counter Chronograph. The time interval between the pulses from Schlieren No. 1 and the interferometer photo-multiplier tube, Δt_d, was measured. The shock distance, S, was computed by

$$S = U_s (\Delta t_d) - 70 \text{ in.} - \frac{c}{2}$$

and then s as before.

Three reference lines appear in each interferogram. They were formed by three wires located in the interferometer reference beam (the beam that does not pass through the test section) at an optical distance from the camera equal to the distance to the center of the test section.

SECTION III

RESULTS

In this section the computations required to determine the density distribution of the flow about the test airfoil from interferograms are described. The means of deducing the pressure distribution on the surface of the airfoil from the density distribution is then explained. The resulting pressure forces are summed to give lift coefficient, pressure drag coefficient, moment coefficient, and center of pressure, and these results are presented. An outline of each of these steps is given in the following subdivisions.

3.1 Measurement of the Density Distribution

In this discussion of the determination of the density distribution about the airfoil, interferometer theory will not be explained. This theory is given adequately in numerous places in the literature (see reference 12, for example). Instead, the point of view adopted here is (a) first to assume that one already has available the required interferograms, then (b) the mechanics of using these available interferograms to determine the density at any point in the flow field will be explained.

In the present series of tests, the interferometer was initially adjusted, before shock-initiated flow was produced, in either of two ways. For one of these two initial adjustment conditions, a pattern of parallel straight light and dark lines (called fringes) is seen on the camera screen. This straight parallel fringe pattern is seen if the density of the gas in the test section is uniform throughout, in particular before shock arrival when there is no flow in the test section. Also for this condition to be observed, the optical elements of the interferometer must be perfect and the test section windows

must be of uniform optical thickness. This adjustment of the interferometer is called the finite fringe adjustment since the width of each fringe seen on the screen is finite. The second of these two initial adjustment conditions, for no flow, is brought about by adjusting the optical elements of the interferometer in such a way that the width of each of the fringes (previously) seen on the camera screen is made infinite. In other words a single (light or dark) fringe is made broad enough to cover the entire camera screen. This is called the infinite fringe (width) adjustment, and the camera screen is either entirely light or entirely dark. In the following paragraphs, the means of using infinite fringe interferograms supplemented by finite fringe interferograms to determine density distribution in a two-dimensional flow field will be discussed. How such interferograms are used will be explained but why they appear as they do will not be treated. For this latter problem, the reader is referred to reference 12.

Since infinite fringe interferograms were used for the most part in the present study, their features and use will be explained first. Figure 12a shows a typical no-flow infinite fringe interferogram where a model is mounted clamped between the test section windows. Ideally a no-flow infinite fringe interferogram should show a field containing no fringes (the screen should be either entirely light or entirely dark). However, stresses produced in the glass as a results of clamping the model between the test section windows cause the fringe bands shown immediately adjacent to the model to appear. In the upper left hand portion of the field of view, there appears another fringe which occurs because the test section windows are not of exactly uniform optical thickness over the entire field of view. Each such line may be regarded as an initial fringe "error" (compared to the ideal no-flow interferogram).

In Fig. 12b, a typical infinite fringe interferogram with flow in the test section is shown. Each light (or dark) line represents the locus of constant density averaged across the test section. These isodensity lines are often referred to as isopycnics. Adjacent light bands represent flow density levels which differ by a known amount (which is to be discussed later). Whether a given fringe represents a greater or lesser density level than its neighbor can not in general be determined from an infinite fringe flow interferogram itself. To settle this question, either theoretical information or a finite fringe flow interferogram of the flow in question is usually used.

Before discussing the mechanics of using the infinite fringe interferograms for density distribution evaluation, the finite fringe no-flow and flow interferograms will be examined. Figure 12c shows a no-flow finite fringe interferogram. Observe that the fringes do not present a perfectly straight and parallel pattern which would be obtained in the ideal case as discussed earlier. The deviations from a straight and parallel pattern arise once again because of model clamping effects and non-uniform optical thicknesses of the test section (and compensator) windows. These initial errors can obviously be assessed throughout the field of view in terms of the deviation of any given fringe from an ideal straight fringe. This finite fringe error assessment can be used to specify the initial fringe "errors" on the infinite fringe no-flow interferogram since these errors are independent of the initial adjustment condition of the interferometer itself.

When the test section is pressurized to effect a density increase, a given (finite) fringe is observed to shift to the right (for a given initial adjustment condition); conversely, when the test section is partially evacuated, that fringe is observed to move to the left. The fringe movement, of course,

is in a direction normal to the original orientation of the fringe pattern. For this adjustment of the interferometer, when there is a variable but continuous distribution of density across the test section (increasing ,say, from the top to the bottom of the field of view), a given fringe would be seen to bend to the right when proceeding from the top to the bottom of the field of view. It is by this (finite fringe) means that one can determine whether in the infinite fringe flow interferogram the density level at a given isopycnic is greater or less than that of its neighbor.

Figure 12d shows a finite-fringe flow interferogram. Using the above information, one can determine using any given fringe whether the density at any point on that fringe is greater or less than that at any selected reference point on that same fringe. It should be recognized that the finite fringe flow interferogram includes essentially the initial fringe error as well as fringe distortion due to the presence of a flow field which has a nonuniform density distribution. The initial error, being perhaps the largest error in the flow interferogram, is subtracted from the flow interferogram in the evaluation of the flow field density distribution. In the present experiments, only the fringe error distribution about the model surface itself is of interest since airforces acting on the model itself are to be deduced; the remainder of the flow field is of secondary interest.

Consider now the mechanics of using the infinite fringe flow interferograms for density distribution evaluation. In practice the fringes on the flow interferogram are numbered (N" say) consecutively from an arbitrary value (100, for example) proceeding around the airfoil. This number applies to the lightest part of a given fringe; this is termed the fringe maximum or "center". In a flow field where the density distribu-

tion is continuous, a neighboring fringe has a number one greater or one smaller than its neighbor. When this numbering has proceeded entirely around the airfoil, the member assigned to the "starting" fringe must check, otherwise an error in numbering has been made. The fringes are numbered, for convenience, in such a way that the higher numbers correspond to locations of higher density levels. This can be done from theoretical considerations or by reference to a corresponding finite fringe flow interferogram, as described earlier.

In practice it is assumed that the flow density at some distant point from the body in the field of view is free-stream density ρ_2; this point is so selected that a fringe numbered N' passes through it. The density on any other isocypnic numbered N'' is then given by

$$\rho_{N''} = \rho_2 + \frac{\lambda}{Lk} (N'' - N') \qquad (3.1)$$

where

- ρ_2 is free-stream density
- N' is the number of the fringe (isopycnic) at which the density level is ρ_2
- N'' is the number of the fringe for which the density level is being sought
- λ is the wave length of the monochromatic light used to make the interferogram (in the present experiments a 40 Å-wide band centered at λ =4481 Å was used)
- L is the width of the test section (8 inches in these tests)
- k is the Gladstone-Dale factor (this is treated as a constant and will be discussed later)

Using Eq. 3.1, the density level for each contour in the field

can be determined. An error of five fringes in selecting that to which free-stream density would be assigned resulted in an error of only one per cent in the lift coefficient of the airfoil. From such a numbered flow interferogram, the fringe number distribution (or the density distribution) over both the top surface and the bottom surface is readily determined.

By a similar numbering of the initial error fringes about the airfoil, the fringe error distribution on both the top surface and the bottom surface of the airfoil can be determined. This distribution can then be applied to remove the "initial error" from the distributions given by the flow interferogram. However, due to the lack of sufficient points for determining an accurate initial error distribution over the airfoil surface, there is an uncertainty of approximately 1/4 fringe in this evaluation. Because of transient stress relief in the glass during a test run, the error distribution on each surface is expected to change; however, the error fringe <u>difference</u> across the airfoil from top to bottom is expected to be nearly unchanged. This <u>difference</u> is the important quantity.

The Gladstone-Dale factor k used in Eq. (3.1) is known to be a function of the wave length of light used as well as the specific humidity and the temperature of the testing medium (air in the present case). The following specific relation for k was taken from references 13 and 14:

$$k = \frac{n-1}{\rho} = \frac{\dfrac{(n-1)_0}{1+.002056(T-492)}\left[\dfrac{1+1.241p\cdot 10^{-4}}{1.001824}\right] - 41\left[\dfrac{1.608\tilde{s}}{1+1.608\tilde{s}}\right]10^{-6}}{\dfrac{1.233(1+\tilde{s})}{T}} \qquad (3.2)$$

where

$(n-1)_o$ = index of refraction minus one for air at 0° C and 760 mm Hg (taken to be 296.34×10^{-6} for λ = 4481 Å)

T = air temperature, °R (free-stream temperature may be used)

p = air pressure, psi (free-stream pressure may be used)

$\bar{s}$ = specific humidity of the test gas (air) being studied, lb. moisture/lb dry air.

ρ = air density, slugs/cu.ft.

Although k varies only about 1 per cent over a wide range of p and T, it was always computed for the particular values of p and T involved. A relative humidity of 50 per cent was assumed for all tests; this effects an uncertainty in k (and ultimately $\Delta\rho$, defined below) of, at most, 1 per cent. A slightly revised form of Eq. 3.2 has been arrived at following a literature search, and will be reported in reference 9, but the correction to Eq. 3.2 is negligible. It should be remarked that the determinations of k found in the literature were made at room temperatures, whereas the temperature behind the shock in the present series of tests was about 100°F above room temperature.

In regard to the two-dimensionality of the flow field, it is desired that the flow properties measured be those in a region of the airfoil that is unaffected by the shock-tube wall. The interferometer, on the other hand, measures an average test-section density from wall to wall. A boundary layer forms on the shock-tube walls behind the incident shock and, with dissipation and conduction to the surface (the wall temperature is less than the free-stream temperature behind the shock), the density near the surface (of the window through which the flow

is being viewed) differs from the "free-stream" value. An estimate, based upon measurements made at $M_2 = 0.16$ and reported in reference 15, indicates the correction to the measured density, to remove the shock-tube wall boundary-layer effect, in the absence of an airfoil, is less than one per cent. These latter measurements will be repeated in the near future at $M = 0.4$, but the effect is expected to remain small. However, it is important to note that the influence of the shock-tube wall boundary layer, including the rest of the boundary at the test section, upon the flow over the airfoil may be important, and will be discussed below.

Before concluding the discussion of the density distribution evaluation, a few additional remarks should be made with reference to the utility of finite fringe flow and no-flow interferograms. Figure 12c shows a no-flow finite fringe interferogram; the density of the air in the test section is ambient (room) density. Figure 12d shows a finite fringe interferogram of flow where the mean flow density is considerably above ambient. In (d) not only have the fringes shown in (c) shifted to the right, but each fringe is distorted because of nonuniform density of flow in the test section. Let the fringes in picture (c) be numbered consecutively from right to left. In the flow interferogram, (d), also let the fringes be numbered consecutively from right to left, where the number of a given fringe (N_r, say) in (c) is retained in (d). The position to which a given fringe in (c) shifts when picture (d) is taken can be determined by white-light fringe identification technique described in reference 12. At any given point P in the flow field (or interferogram), the difference in density between conditions in pictures (c) and (d) is given by

$$\rho_{P_{(d)}} - \rho_{P_{(c)}} = \frac{\lambda}{Lk} \left[N_{P_{(d)}} - N_{P_{(c)}} \right] \qquad (3.3)$$

where

$\rho_{P_{(c)}}$ is the flow field density at point P in Picture(c)

$\rho_{P_{(d)}}$ is the flow field density at the same point P in picture (d)

$N_{P_{(c)}}$ is the number of the fringe passing through point P in picture (c)

$N_{P_{(d)}}$ is the number of the fringe passing through this same point P in picture d, and

the remaining quantities are as defined following Eq. 3.1. Since the no-flow density is known, Eq. 3.3 permits the complete density distribution throughout the field of view to be determined. This method is tedious; on the other hand, the initial errors are automatically removed in this evaluation.

3.2 Calculation of the Pressure Distribution and the Aerodynamic Coefficients

3.2.1 Entropy About the Airfoil During Shock Passage

To compute the pressure distribution on the airfoil, it is necessary to determine, in addition to the density distribution, the entropy distribution. This will be discussed with reference to Fig. 13. The entropy is established primarily by the flow-initiating shock which is plane, until it reaches the airfoil, creating a two-dimensionally uniform entropy field. As the shock diffracts about the fore portion of the airfoil, Mach reflection takes place because of the inclination of the surfaces and strength of the shock involved, making the shock curved along a portion adjoining the airfoil surfaces. Compression waves emanate from the top and bottom surfaces (at $\alpha > 5.7^{o}$ both compression and rarefaction waves radiate) while the shock is passing over the fore semi-chord of the airfoil. Within a nearly triangular zone above, and below, the airfoil, the fluid has passed through the diffracted and hence curved portion of

the shock, and is therefore rotational. The irrotational and rotational regions are separated by a so-called slip surface, which has been examined analytically by Ting and Ludloff [8].

The problem is to determine the surface pressure in this rotational region. The isopycnics (isodensity lines), which are smooth in the irrotational region, have a "break" at the slip surface (a very steep density gradient over a thin strip, according to reference 8) and depart from the isobars (isopressure lines). The analysis of reference 8 indicates that there is no appreciable pressure gradient at the slip surface, and that the isobars continue smoothly from the homentropic region to the airfoil surface. Therefore in this region the surface pressure was obtained by extrapolation from outside the slip surface, as shown in Fig. 14a. In runs 34 and 29, Fig. 11, the break in the isopycnic at this slip surface was small when the shock was ahead of the midchord. But in runs 35.2, 35.3, 25.17, and 25.18, the break is well defined, particularly below the airfoil. The uncertainty in the lift, etc., due to this extrapolation method is probably constant percentwise until the shock reaches the midchord, since essentially the whole region grows with space-time similarity.

After the shock passes the midchord, another slip surface forms, which appears in Fig. 11, runs 34.5, 29.7, 35.4, and 25.19, intersecting the airfoil at roughly one-third the distance from the midchord to the shock. Again the isobars must be extrapolated, but the uncertainty in the lift is expected to be about the same percentwise as when the shock was ahead of the midchord.

During the shock-diffraction period, the difference in displacement of the shock on the top and bottom surfaces accounts for about one-third of the normal force at both $\alpha = 4$

and 8.3 degrees. The uncertainty in determining the lift, including the fact that the fringes have a finite spacing and thickness from which a density distribution must be faired, is estimated to be 5 to 10 per cent during this period.

3.2.2 Free-Stream Entropy During Later Period

As the shock moves farther downstream, this rotational flow moves downstream also, and the flow generated upstream by the plane shock passes over the airfoil. Surprisingly very few measurements have been made of free-stream flow field behind the incident shock in a shock tube. Concurrent with the airfoil tests reported herein, a program of measurement of the shock-induced flow is being undertaken and will be reported in the future: for the present, the statements contained herein on the characteristics of this flow field are tentative and primarily qualitative.

In the absence of the airfoil, the incident shock appears to be plane, within the field of view, and the density change across the shock is uniform. Behind the incident shock are a number of weak shocks which have not caught up to the main shock. Within the field of view shown in any one interferogram (5 by 7 inch ellipse in space), the undisturbed flow is believed to be reasonably uniform, but during the duration of the experiment (about 45 milliseconds), the variation from the initial shock-initiated flow condition is evidently considerable. At present the variation in flow is not known sufficiently reliably to present as a final correction to the data, so the data will first be presented assuming the flow is a step function generated by a single plane flow-initiating shock, and the free-stream flow properties behind the shock will be computed from T_1, p_1, and U. The local pressure about the airfoil behind the shock will be computed from

$$p = \left(\frac{\rho}{\rho_2}\right)^{\gamma} p_2 \qquad (3.4)$$

A tentative correction will be made below for the fact that the flow is actually not a step function.

3.2.3 Airfoil Viscous and Thermal Effects on the Entropy of the Flow

In addition to the multi-entropic flow generated during the shock diffraction period, the shock-induced flow is subjected to viscous and heat-transfer effects as it passes over the airfoil surface. Calculations indicate that the airfoil surface also is about 100°F cooler than the free-stream fluid during the experiments reported herein, so the surface fluid would be cooled, as is substantiated by the character of the isopycnics. On the presumption that the thermal and viscous boundary layers are nearly the same thickness, the boundary layer on the under surface is first quite thin, becomes even thinner at the corner, then grows again on the rear half chord of the airfoil. The pressure at the surface of the airfoil was taken equal to the value at the outer edge of the boundary layer, i.e., at the knee of the isopycnics, as shown in Fig. 14b. There was little apparent difficulty in determining the boundary-layer thickness on the under surface.

The determination of the pressure on the top surface is more difficult. For tests in which airfoil angles of attack are 4° and 8.3°, a vortex forms behind the leading edge, and is quite strong by the time the shock reaches the trailing edge. Two problems arise. The first is the determination of the surface pressure in the region of the vortex. Again it is quite probable that the pressure at the surface does not correspond (i.e., using Eq. 3.4) to the isopycnic at the surface, since there are undoubtedly viscous effects due to the surface. But

it is not clear how viscosity enters in this region. Furthermore in many interferograms (e.g., Fig. 11, run 35.7), the fringes are obscure near the surface in this region. For want of a more rational procedure, the pressure at the surface was generally taken equal to the (isentropic) pressure of the isopycnic tangent to the surface normal, as shown in Fig. 14c. This gives pressures that are somewhat lower than if the surface isopycnics were used. But the difference in the lift coefficient, C_L, is less than 5 per cent, tending to be larger, except at 8.3° for large values of s/c.

The second problem is the effect of the vortex on the determination of the downstream pressure. The fluid that is outside of the apparent rear-surface boundary layer has passed through the region of large pressure gradients near the leading edge vortex region, and a question arises as to its entropy. The growth of the leading edge vortex region and the detachment of portions which sweep downstream is quite striking in the interferograms of run 35, Fig. 11. Quite a clear picture of the entropy of the flow outside the boundary layer on the upper-rear surface can be reached by the following comparison. First, the flow on the under surface is subject to much gentler pressure gradients. So, compared to the flow above the airfoil, it is reasonable to presume its entropy variation is small. Secondly, after the flow leaves the trailing edge, the streamline curvature is expected to be small. Therefore, an isopycnic in the upper region behind the airfoil should be able to be extended smoothly through the "thermal" wake into the same isopycnic in the lower region (see Fig. 14d, and run 35.8 of Fig. 11). Departures of the density across the thermal wake would indicate that the entropy of the flow above the thermal wake differs from that below the wake. At 4° the agreement of the density across the thermal wake after runs 29.11 and 35.6,

roughly for $s/c > 1$, is very good, or the difference in entropy of the flow on either side of the "thermal" wake is negligible. At 8.3° the agreement is good for runs 25.23 - 25.25, or $1.09 < s/c < 2.03$, but thereafter the departure from isentropic behavior is roughly two fringes. This latter period is when the viscous effects become large, and in fact the flow may actually be separated locally. The wind-tunnel lift data of Bartlett and Peterson [16] indicate separation at this angle. Apparently a lower-bound estimate of the lift is achieved by increasing each fringe value on the upper surface by two, accounting for the above two-fringe departure; this results in a reduction C_L of 25 per cent. If it is assumed that there is no entropy variation around the airfoil, the pressures obtained from the observed densities provide an upper bound on the lift acting on the airfoil. The actual value is expected to be somewhere between the two. At any rate the bounds of the experiment where the isentropic assumption is valid appear clearly defined and a limiting estimate of the departure from isentropic conditions can be made. In order to determine the surface pressure more reliably for cases where the entropy is not constant, a program has been embarked upon to measure the surface pressure directly.

It should be recalled that one would expect the entropy of the upper-surface fluid to be less than the under-surface fluid behind the airfoil before the slip surface has passed the trailing edge. This appears to be confirmed in Fig. 11: runs 29.10, 29.11, and 25.22.

3.2.4 Summary of Steps to Determine the Pressure Distribution

Specifically then the airfoil pressure distribution was determined as follows:

1. The fringes were numbered; the larger values corresponding to the greater densities.

2. A fringe, well away from the airfoil, numbered N', was selected as that corresponding to the free-stream value of the density. For the free-stream properties (density and pressure), the values computed immediately behind the shock (see Section II) were employed.

3. The density at other points was found by Eq. 3.3, and the pressure outside of the airfoil boundary layer, by assuming the process to be isentropic (Eq. 3.4).

4. The pressure at the surface was taken equal to the pressure outside the boundary layer as described above.

3.2.5 Computation of the Aerodynamic Coefficients

The pressure coefficient was computed and defined as

$$C_p = \frac{p - p_2}{\frac{1}{2} \rho_2 u_2^2}$$

and the profiles at representative delay times are shown in Fig. 11. From the C_p profiles were computed the pressure-drag coefficient, C_{D_p}, the lift coefficient, C_L, $C_{L/C_{D_p}}$, the moment coefficient about the midchord, $C_{M_{c/2}}$, and the chordwise distance of the center of pressure from the leading edge, c.p., nondimensionalized by c. The values of the aerodynamic coefficients are shown in Fig. 15 as a function of the chord lengths travelled by the (ideal) flow behind the shock after the shock reached the leading edge of the airfoil; these chord lengths are defined by $u_2 t/c$.

3.2.6 Tunnel-Wall Corrections

According to the steady-flow correction methods given by Pankhurst and Holder, ref. 17, the aerodynamic coefficients

would be generally reduced by about one per cent, the largest correction being 2 1/2 per cent for $C_{M_{c/2}}$ at $\alpha = 8.3^{\circ}$. These corrections are much less than the other experimental uncertainties, so they were not incorporated. There is also a question as to the effect of the wall interference during the transient period. Certainly there would be no interference before $\frac{s}{c} \doteq 2$ when the first waves generated by the diffraction of the incident shock over the airfoil would reflect from the walls. No clear evidence of such an interference was observed, and the correction is expected to be small in view of the radial growth and consequent rapid weakening of these waves. Therefore, an interference correction was not attempted during the transient period.

SECTION IV

DISCUSSION

The transient period will be divided into two parts for discussion purposes: the first interval $0 < \frac{S}{c} < 1$ ($s = .34S$ at $M_2 = 0.4$) will be called the diffraction period, followed by what is called the post-diffraction period. The separation is made since the shock and the associated waves are of prime importance in the diffraction period, in contrast to the later times where the flow development about the airfoil corresponds roughly with the airflow growth for an airfoil subjected to a sharp-edged gust in compressible flow. The separation between the two parts is not sharp since shock interaction occurs at the trailing edge after $S/c = 1$, and the rotational flow generated by the Mach shocks leaves at about $S/c = 3$ at $M_2 = 0.4$.

4.1 Diffraction Period

4.1.1 Aerodynamic Coefficients

During this period the aerodynamic coefficients behave in a simple manner. While the shock is ahead of the mid-chord, $S/c < .5$ ($s/c < .16$), neglecting viscous and heat transfer effects there is no fixed characteristic length so the flow is correctly similar. It is observed in Fig. 15a through Fig. 15j that C_L, C_{D_p} and cp/c increase linearly and $C_{M_{c/2}}$ is parabolic, with a maximum at $s/c = .135$, this linear behavior supports the negligible influence of viscous and heat transfer effects during the early flow development. One-third of the lift is contributed by the displacement of the under-surface shock ahead of the upper-surface shock, at both 4^o and 8.3^o. The large drag when the shock is at the mid-chord should be noted.

While the shock is passing from the mid-chord to the trailing edge, similarity no longer applies for there is now a

fixed characteristic length in the flow--the distance from the leading edge to the corner of the semi-chord. Nevertheless, the displacement of the lower shock ahead of the upper shock continues to increase essentially linearly and still accounts for one-third of the lift, and the continued linear increase in C_L is a good approximation to the data. That C_L tends to continue the linear rise of the $0<\frac{S}{c}<\frac{1}{2}$ data is reasonable if one notes the following. The shock adjacent to the lower surface is weakened after it pasces the midchord because of the change in direction of the surface. Therefore, the pressure behind the shock is also less in this region. But the top surface also "pulls back" by the same amount anglewise so that the surface pressure behind the upper-surface shock, to a linear approximation, is reduced the same amount, preserving the linear rise in C_L.

A two-valued pressure field divided by a plane front moving at the undisturbed-shock velocity U, (pressure p_1 ahead and pressure p_2 behind the front) would produce a C_{D_p} history on the airfoil at small angles of attack according to the dashed line in Fig. 15c until the shock reaches the trailing edge. This agrees well with the data, except at 8.3° for $1/2 < S/c < 1$ where the experimental values are larger.

The most striking feature of the airforces during the diffraction period is the large negative moment as the shock approaches the trailing edge. The linear lift representation of Fig. 15a gives the parabolic $C_{M_{c/2}}$ curve in Fig. 15g, with the intercept at $s/c = 0.27$ and reaching a minimum at $\frac{s}{c} = 0.33$.

4.1.2 Analyses

For reasons mentioned above (section I), the blast-wave analysis of Ting and Ludloff, reference 8, was not compared. A comparison is advised, with the intent of extending the analysis

to include curvature of the stagnation streamline. But more important it may give an insight into the problem of a moving airfoil penetrating a blast wave, to be extended to the case where the blast wave approaches from an arbitrary angle.

For engineering purposes the geometric approximation of a parabolic Mach Shock normal to the surface and tangent to the incident shock at a point moving with the sonic speed behind the shock was examined, Fig. 16. The displacement between the shocks agrees well with experiment, but assuming a simple surface pressure behavior, specifically, that it be equal to the value at the shock-surface intersection resulted in a value of lift which differed from the experimental value by a factor of six. However, it might still be worth while to attempt other simple curves for the surface pressure distribution for engineering purposes.

For the sake of completeness, the analysis of Mazelsky and Drischler [6] for the lift of a flat plate penetrating a sharp-edged gust was compared in Fig. 15a by fairing their data of $M = 0$, 0.5, 0.6, and 0.7 and interpolating for $M = 0.4$. It is evident that this model differs significantly in the early stage of the actual flow. Roughly half of the difference is accounted for by the lift due to the horizontal displacement between the shocks on the upper and lower surfaces, and the balance is presumably due to the inherent difference between the shock and gust penetration problems.

Quite interesting is the comparison of the analyses by Hobbs [7] (see Section I), which applies to a flat plate in an incompressible flow. The horizontal velocity of the airfoil in this analysis is constant, and was taken equal in the present calculation to the value corresponding to $M = 0.4$. The velocity of the gust front was taken equal to the shock velocity at $M_2 = 0.4$, the initial $\alpha = 4^{\circ}$. The computed curves for C_L,

Fig. 15a, have maxima in the diffraction period that are nearly equal to the maxima of the shock tube data, although displaced timewise. The hump in the former case is an apparent-mass effect.

4.1.3 Importance of the Diffraction Period

A few remarks will be made here to start the thinking on the outcome of the present experiment, but it must be emphasized that this is not intended to be a critical evaluation, which would be a separate study. A short wing-bending period is on the order of 100 milliseconds. A shock of the present magnitude would pass over a 6-foot chord in about 4 ms. Therefore, the particular shape of the C_L curve in the defraction period would not be significant to bending. On the other hand, a torsion period may be as low as 10 ms. But $C_{M_{c/2}}$, which has a large maximum and minimum value in the diffraction period, would have a 3 ms. "half-period" so the shape of its curve could be important. Of course, the stiffness in torsion is greater so that torsion might not be important. This would have to be examined. It is believed the same conclusions would apply to a horizontal tail. In addition to these overall effects, the local effects due to the large pressure rise across the shock could be important to wing skins. When this pressure rise is coupled with the displacement between the upper and lower-surface shocks it may induce some effect on movable surfaces. In other words, the large force on the trailing edge that made the moment even go negative when the shock approached the trailing edge, would be acting locally on the movable surfaces, and could be important.

4.2 Post-Diffraction Period

4.2.1 Variation of "Free-Stream" Dynamic Pressure in the Shock-Initiated Flow

The aerodynamic coefficients at large delay times as origi-

nally computed on the basis of a step-function flow field, Fig. 15, were considerably larger than wind tunnel data, as shown in Fig. 17. The steady-state data of Bartlett and Peterson [16] were obtained with a 3-inch chord, 3-inch span model spanning a 3- by 16-inch closed tunnel at R_e = 820,000 and were reduced by 8/9 to convert from 4.5° to 4°; and the data of Humphreys [18] with a 4-inch chord 4-inch span model spanning the Langley 4- by 19-inch semi-open tunnel, and are an interpolation of the values at M = 0.31 and 0.48. Both measured the surface pressure directly. The portion of the present data which is used for this steady-state comparison is an average value of that for $20 < s/c < 52$. At angles of attack of 4 and 8.3° the present C_L data (based on the ideal step-function flow field) were respectively 58 and 48 per cent larger than the curve representing references 16 and 18.

A great deal of effort was made to account for the difference on the basis of thermal effects due to the cooling of the boundary layer by the airfoil. This effect may be important. But there has been growing recognition in the past several years by shock-tube investigators of the departure of the real shock tube flow profile from the ideal step-function (e.g., see reference 19). The mechanism whereby the actual flow is caused to deviate from the ideal step function is not as yet completely understood, but it appears to be due to a combination of the boundary layer forming on the shock-tube wall between the shock and the head of the rarefaction wave, and the irregular rupture of the diaphragm. The latter is expected to be the major factor in a shock tube of the present large cross-section. Many of the interferograms in the present tests have shown weak shocks that have not yet overtaken the initial flow-initiating shock. Several are indicated in Fig. 11.

Exploratory pressure and temperature measurements were made in this shock tube of the flow following the shock passage with

the shock tube empty. But the most reliable measurements are the numerous white-light interferograms taken both as single-spark exposures at various delay times and also strip film with a continuous light source. These were made over a wide range of P_{21} and employing various diaphragm materials, as a portion of a program to calibrate the flow in the shock tube. The particular measurements to be discussed were made at the conditions of the present experiment ($M_2 = 0.4$, same Reynolds number, etc.). As mentioned above, the interferometer measures an average density across the test section from window to window. But, at present, based on the data of reference 15, it appears that the effect of the shock tube wall boundary layer is negligible, so essentially the interferograms represent the free-stream density behind the shock, $\tilde{\rho}$.

In order to compute a free-stream dynamic pressure, $\tilde{q}$, from $\tilde{\rho}$, two flow models were postulated. Model A assumes that a single second shock follows the initial shock to give the observed change in stream density, and Model B assumes an infinite number of infinitesimal trailing shocks. For a mean value of the $\tilde{\rho} / \rho_2$ data at a delay time corresponding to $s/c \approx 60$, $c = 4$ in., both models agree on $\tilde{q}/q_2$ within 0.3 per cent.

A curve was faired through the $\tilde{\rho}$ data, and $\tilde{q} / q_2$ was computed, Fig. 18, employing Model B. The delay time was converted to s/c with c = 4 in., and the curve, for the present, applies only to the conditions of this experiment. The curve is considered tentative in view of: (1) the large spread in the data, indicated by the shaded area in Fig. 18 together with the limited data available, and (2) the need to substantiate the relation between $\tilde{\rho}$ and $\tilde{q}$. It is perhaps significant that the rise in $\tilde{q}$ from $s/c = 0$ to $s/c = 10$ is rapid, 10 per cent, with a comparatively small scatter in data.

The aerodynamic coefficients were corrected on the basis of a quasi-steady flow field by using $\tilde{q}$ as the dynamic pressure, and are shown in Fig. 18. The correction is negligible for $s/c < 1$. The correction brought the average C_L value in the interval $20 < s/c < 52$ into good agreement with the flat-plate values, but they are still 30 and 24 per cent larger than the wind-tunnel data at 4^o and 8.3^o, respectively, Fig. 17a. The remaining differences may reflect the effect of: (1) heat transfer, (2) "free-stream" turbulence and trailing shocks, (3) the shock-tube boundary layer on the flow as it passes over the airfoil, or, of course, (4) the values of $\tilde{q}$. It should be emphasized at this point, that although items (1), (2) and (3) may prove to be real differences between the flow over bodies in a shock tube and in a wind tunnel, item (1), and perhaps (2), makes the shock-tube flow a more real comparison to an actual flow behind a blast.

4.2.2 Aerodynamic Coefficients

After the lower shock diffracts around the trailing edge to the top surface, the two shocks intersect and a vortex forms whose axis is above the airfoil, Fig. 11, runs 29.8-.9, 35.5, 25.21-22. The nature of this vortex is not known as its origin is in a rotational region, which must be realized in comparing to the well-known starting vortex (in incompressible flow), which is in an irrotational flow field. There is even a question as to the sense of the vortex.

Concurrently a compression wave moves forward on the upper surface and an expansion wave moves forward on the lower surface, tending to hasten the readjustment of C_L, $C_{M_{\frac{c}{2}}}$, and $\frac{cp}{c}$. By $s/c = 0.7$ these waves have reached the leading edge, and the experimental C_L values compare more nearly to the gust-response values of references 6 and 7. The agreement is better at $\alpha = 4^o$.

We will not attempt to describe the response further, except to note the following.

The C_L values have a peculiar hump in the $1.5 < s/c < 15$ range in comparison to the two gust analyses, Fig. 17a. The hump is more prominent in the 8.3^o angle of attack case. This may represent the delay time for (local) separation. Otherwise there is only a slight preference for the C_L values of reference 6 in comparison to those of references 7 in this region. The $C_{M_{\frac{c}{2}}}$ data rise smoothly at 4^o, but oscillates at 8.3^o in the $1.5 < s/c < 15$ region, which may also be associated with separation. Unfortunately there is no direct means for detecting separation from the interferograms, although the difference in the fringe number of the upper- and lower-surface flow at the trailing edge, as discussed in subdivision 3.2.3, indicate that separation may have existed at this delay time.

4.3 Examination of the Steady-State Flow

4.3.1 Comparison to Wind-Tunnel Tests

The C_p distribution of run 29.22 at $\alpha = 4^o$ and $s/c = 47.6$, where the flow is believed to have reached a steady-state is compared to the steady-state wind-tunnel data in Fig. 20. Both the uncorrected and $\tilde{q}$-corrected MIT data are shown. The latter data will be discussed. All four profiles are matched at $x/c = 0.2$ on the lower surface, where x is the chordwise distance from the leading edge. The data agree well on the lower surface to $x/c = 0.55$. From there on the shock-tube pressure data level off at a value that the wind-tunnel profiles indicate is below the free-stream pressure. This difference is not understood, although the profile is confirmed by other shock-tube pressure-distribution profiles at the late delay times.

On the upper surface the data of reference 16 agree with the shock tube results until $x/c \approx 1/4$. From there on, save for

a small difference at the midchord, reference 16 is in agreement with reference 18. The shock-tube profiles varied most between interferograms along the first quarter chord on the upper surface, but run 29.22 is typical. Reference 18 observed separation at the nose and shoulder, in agreement with a high pressure on the fore-quarter. It is not clear whether separation occurred at $\alpha = 4^{\circ}$ in the shock tube experiments. The lower pressure in the shock tube behind the quarter chord is at present only explained by a thinner boundary layer on the airfoil than in the wind tunnel. The verification of this pressure difference by direct measurement is important and is one of the next steps in the shock-tube program. A direct measurement at $x/c \approx 0.3$ would greatly clarify the picture.

Unfortunately the conclusions about the comparison between the airfoil flow details in a shock tube and a wind tunnel at present must be limited. The double-wedge shape was employed in these first tests to facilitate the computation of the aerodynamic coefficients. But it is possible that local separation occurred on the upper-forward surface which could be sensitive to leading-edge sharpness, turbulence, etc. Therefore experiments are in progress employing a more conventional shape of airfoil, the NACA 65-010.

4.3.2 Comparison to Schwarz-Christoffel Solution

The one analytical solution to which the present experimental data can be compared is the Schwarz-Christoffel transformation for the double-wedge airfoil in an irrotational, incompressible, and nonconducting fluid in steady-state motion. This is limited to $\alpha = 0^{\circ}$. The Prandtl-Glauert correction $\sqrt{1 - M^2}$ was applied to the S-C solution, which was then converted to the local fringe number by the Gladstone-Dale relation, in order to effect a direct comparison to the experimental data.

This is shown as the solid curve in Fig. 21: the necessary fluid properties correspond to immediately behind the shock. Since the variation in the free-stream flow behind the shock from a step-shock would affect this comparison, the results of the S-C analysis were also converted to fringe-number distribution by using the $\tilde{q}$-correction at $s/c = 52.3$, corresponding to run 34.20. This is the dashed curve in Fig. 21. The experimental fringe data were taken from run 34.20. The data were all corrected by a small fixed amount to match the theoretical curves at $x/c = 0.15$.

Run 34.20 is in good agreement with the S-C solution over most of the airfoil. The difference at the leading edge is due to the slight deviation of the flow direction from horizontal, which from picture to picture was randomly inclined up and down. Humphreys [18] had compared the wind-tunnel pressure measurements to the S-C results, and found a tendency of the measured data to be high near the midchord. This result, when interpreted to the MIT data, tends to support the validity of the tentative $\tilde{q}$-correction. The leveling of the data at $x/c = 0.65$ may indicate a rapid growth of the boundary layer in this particular photograph. There were no indications of separation. In some interferograms, the density at the trailing edge was greater than at the leading edge; there was no regularity. But an average over many interferograms would give a more symmetrical distribution about the midchord. The pressure measurements of references 16 and 18, which are time-average values, were quite symmetrical about the midchord.

SECTION V

CONCLUSIONS AND RECOMMENDATIONS

1. There is a sufficient duration of flow in the M.I.T.-W.A.D.C. shock tube before the arrival of the contact surface or reflected shock at $M_2 = 0.4$ and $Re \sim 10^6$ to produce evidently a steady-state flow condition around the airfoil.

2. The deviation of the flow, without a model present, from a step-function flow field is significant. Interferograms indicate a "free-stream" dynamic pressure, q, increase of 30 percent in 40 milliseconds ($\frac{s}{c} = 60$). An important phase of the future investigation will be the measurement of the flow properties following the shock passage. A tentative quasi-steady correction (called $\tilde{q}$-correction) was applied. The direct measurement of the initial temperature, T_1, or speed of sound, a_1, before shock arrival is recommended in such experiments.

3. During the period of shock diffraction about the airfoil, the aerodynamic coefficients are well represented by simple curves. The most striking feature is the large moment reversal at $\alpha = 4^\circ$ and at $\alpha = 8.3^\circ$ when the shock is near the trailing edge. The displacement of the lower-surface shock ahead of the upper-surface shock contributes one-third of the lift. No complete analysis of the forces acting on the airfoil during shock diffraction exists for the case in which the shock-initiated flow is subsonic. But it is recommended that a comparison be made employing the method of reference 8, with the intent of extending the method to include curvature of the stagnation streamline, and eventually including a moving airfoil with a shock approaching the moving airfoil at an arbitrary angle (see Sub-Division 4.1.2).

4. Following shock passage there is a rapid readjustment of the

aerodynamic coefficients to the gust-type response. There was a slight preference for the results of reference 6 in contrast to those of reference 7, but both differed significantly from the experimental results in the interval $1.5 < \frac{s}{c} < 15$.

5. The steady-state values of C_L after the $\tilde{q}$-correction agree well with flat-plate theory (isentropic), but are still 24 and 30 percent larger than wind-tunnel data at 4^o and 8.3^o respectively. Further examination of the difference will be a part of the future work in order to evaluate the shock tube for steady-state aerodynamic experiments, i.e. a short duration wind tunnel. Tests are in progress with a more conventional airfoil, the NACA 65-010. It would be worthwhile to compare the shock-tube tests to full-scale explosion tests, since, as pointed out in Section 4.2.1, some of the characteristics of the shock-tube flow over bodies that differ from wind-tunnel conditions are characteristics that make shock-tube flow a more real comparison to flow behind a blast.

6. Agreement of the measured density distribution with perfect-fluid (isentropic) theory at $\alpha = 0^o$ is good. Some difference is observed near the midchord, which difference was also exhibited in the wind tunnel.

7. The bounds of the isentropic assumption appear to be clearly indicated. The entropy variation due to the Mach shock and the thermal boundary layer are apparently interpretable so that the surface pressure can be obtained by extrapolation, except at 8.3^o for $\frac{s}{c} > 2$. More questionable is the determination of the surface pressure in the region of the leading-edge vortex. A program is in progress to measure surface pressure directly.

8. A program to improve the method of supporting the model, in order to test at larger angles of attack, is needed and is underway.

9. A large fraction of the effort was devoted to the reduction of the aerodynamic coefficients from the interferograms. A rapid-responding dynamic balance, in combination with interferograms for qualitative examination and a reduced number of quantitative measurements, would greatly reduce the computational man-hours in studies of this type.

REFERENCES

1. Wagner, H., Über die Entstehung des dynamischen Auftriebes von Tragflügeln, Z.f.a. M.M., Bd. 5, Heft 1, s. 17-35, February 1925.

2. Küssner, H. G., Zusammenfassender Bericht über den Instationären Auftrieb von Flügeln, Luftfahrtforsch., Bd. 13, Nr. 12, s. 421, December 1936.

3. von Karman, T., and Sears, W. R., Airfoil Theory for Non-uniform Motion, Jour. Aero. Sci., v. 5, no. 10, Aug. 1938.

4. Lomax, H., Heaslet, M. A., Fuller, F. B., and Sluder, L., Two-and Three-Dimensional Unsteady Lift Problems in High-Speed Flight, N.A.C.A., Rep. 1077, 1952.

5. Mazelsky, B., Numerical Determination of Indicial Lift of a Two-Dimensional Sinking Airfoil at Subsonic Mach Numbers from Oscillatory Lift Coefficients with Calculations for Mach Number 0.7, N.A.C.A., T.N. 2562, Dec. 1951

6. Mazelsky, B., and Drischler, J. A., Numerical Determination of Indicial Lift and Moment Functions for a Two-Dimensional Sinking and Pitching Airfoil at Mach Numbers 0.5 and 0.6, N.A.C.A., T.N. 2739, July 1952.

7. Hobbs, N.P., Mass. Inst. of Tech., (Private Communication).

8. Ting, L., and Ludloff, H. F., Aerodynamics of Blasts, Jour. Aero. Sci., v. 19, no. 5, May 1952.

9. Witmer, E. A., et al, The M.I.T.-W.A.D.C. 8- by 24-inch Shock Tube, (In process of completion).

10. Glass, I. I., Martin, W., and Patterson, G. N., A Theoretical and Experimental Study of the Shock Tube, U.T.I.A., Rep. No. 2, Nov. 1953.

REFERENCES (Continued)

11. Hirschfelder, J. O., and Curtiss, C. F., Therodynamic Properties of Air, II, University of Wisconsin, Dec. 1948.

12. Physical Measurements in Gas Dynamics and Combustion, Vol. IX of High Speed Aerodynamics and Jet Propulsion, Princeton University Press, Princeton, N. J., 1954.

13. International Critical Tables, McGraw-Hill Book Co., Inc., v. II, pp. 1-6, 1930.

14. Edelman, G. M., and Bright, M. M., The Specific Refractivity of Gases for Various Wave lengths of Light, M.I.T., Gas-Turbine Lab. Rep. No. 6, May 1948.

15. Stever, H. G., Witmer, E. A., and Herrmann, W., The Growth of the Boundary Layer Behind a Shock Wave, 50 Jahre Grenzschichtforschung, Edited by H. Görtler and W. Tollmien, Friedr. Vieweg und Sohn, Braunschweig, pp. 272-79, 1955.

16. Bartlett, G. E., and Peterson, J. H., Wind-Tunnel Investigation of Double-Wedge Airfoil at Subsonic Speeds, Bumblebee Rep. No. 53 (Contract NOrd-8993), Cornell Aero. Lab., Aug. 1946.

17. Pankhurst, R. C. and Holder, D. W., Wind-Tunnel Technique, Pitman and Sons, Ltd., London, 1952.

18. Humphreys, M. D., An Investigation of a Lifting 10-Percent-Thick Symmetrical Double-Wedge Airfoil at Mach Numbers up to 1, N.A.C.A., T.N. 3306, Nov. 1954.

19. Trimpi, R. L., and Cohen, N. B., A Theory for Predicting the Flow of Real Gases in Shock Tubes with Experimental Verification, N.A.C.A., T.N. 3375, March 1955.

a. STEP IN ANGLE OF ATTACK
INCOMPRESSIBLE (WAGNER)
COMPRESSIBLE (LOMAX et al)

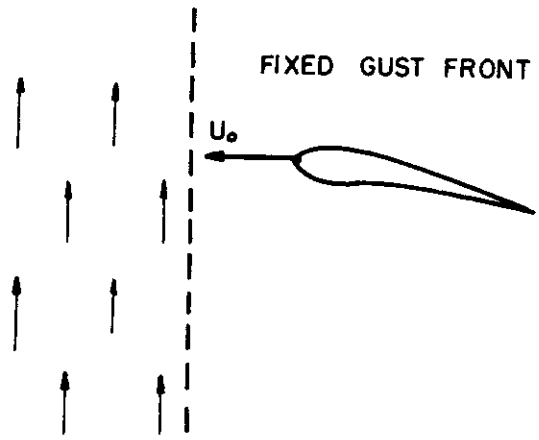

b. PENETRATION OF A SHARP-EDGED GUST
INCOMPRESSIBLE (KÜSSNER; KARMAN & SEARS)
COMPRESSIBLE (MAZELSKY)

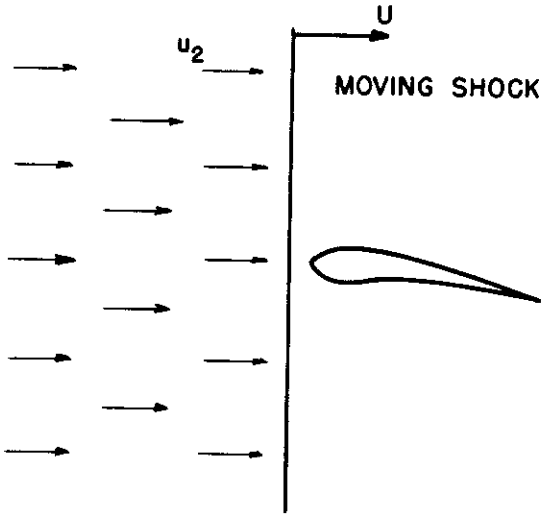

c. PRESENT SHOCK-TUBE TESTS

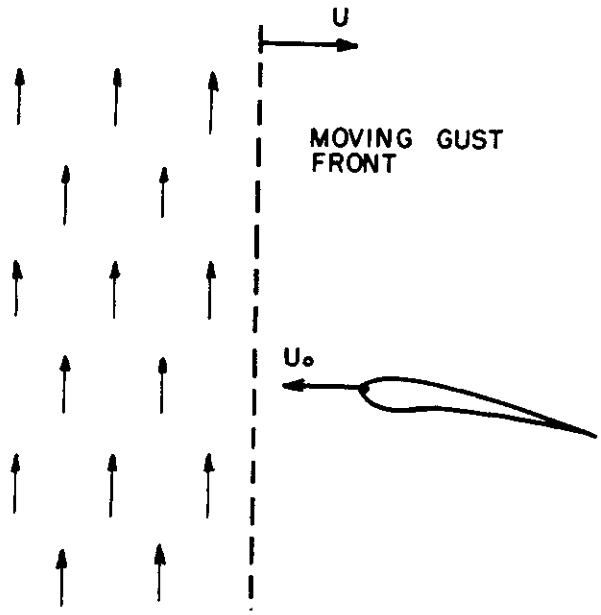

d. MOVING GUST FRONT (HOBBS)

FIG. 1 SCHEMATIC OF SEVERAL TRANSIENT AIRFLOW CASES FOR AN AIRFOIL

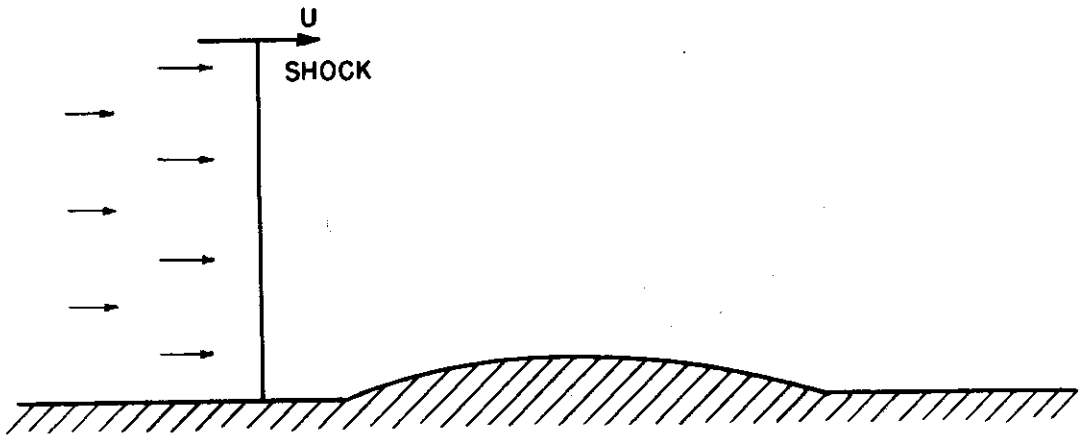

a. PROBLEM ANALYZED BY TING AND LUDLOFF

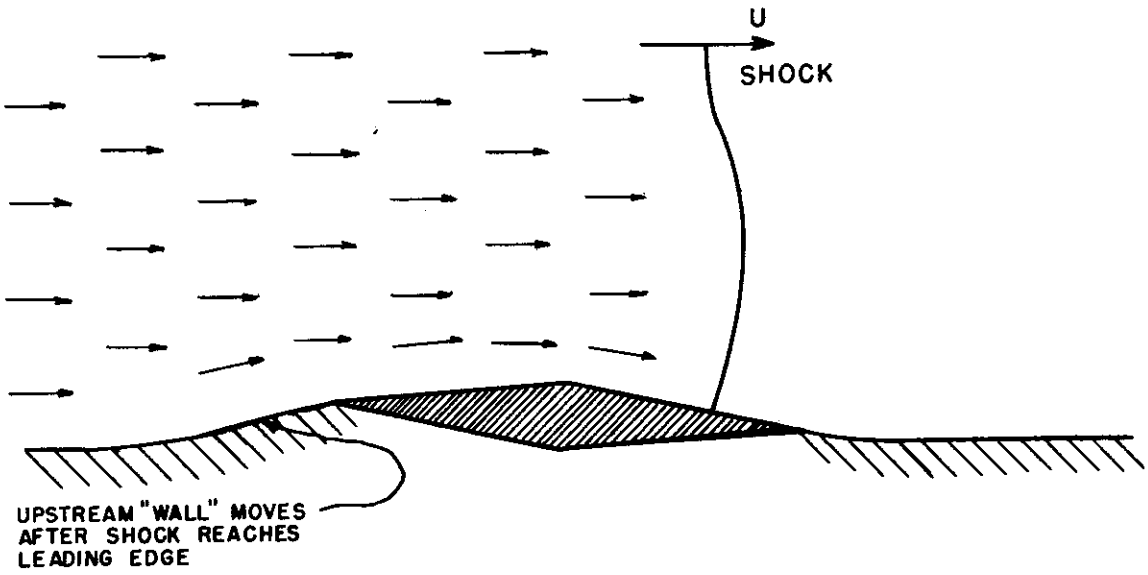

b. APPLICATION TO PRESENT PROBLEM

FIG. 2 COMPARISON OF SHOCK PASSAGE OVER A BUMP ON A WALL, AND OVER AN AIRFOIL

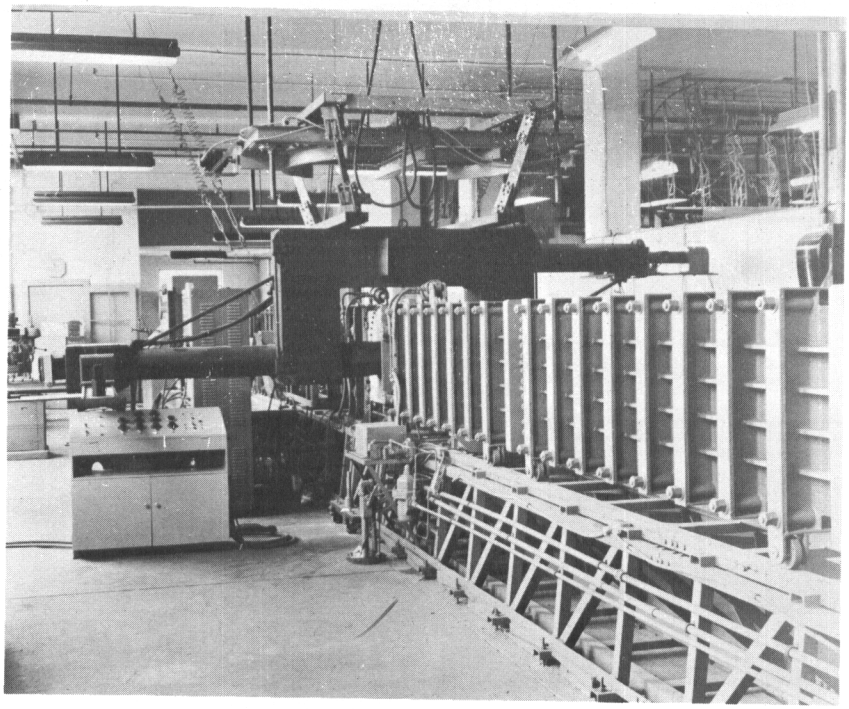

FIG. 3 OVERALL VIEW OF THE SHOCK TUBE

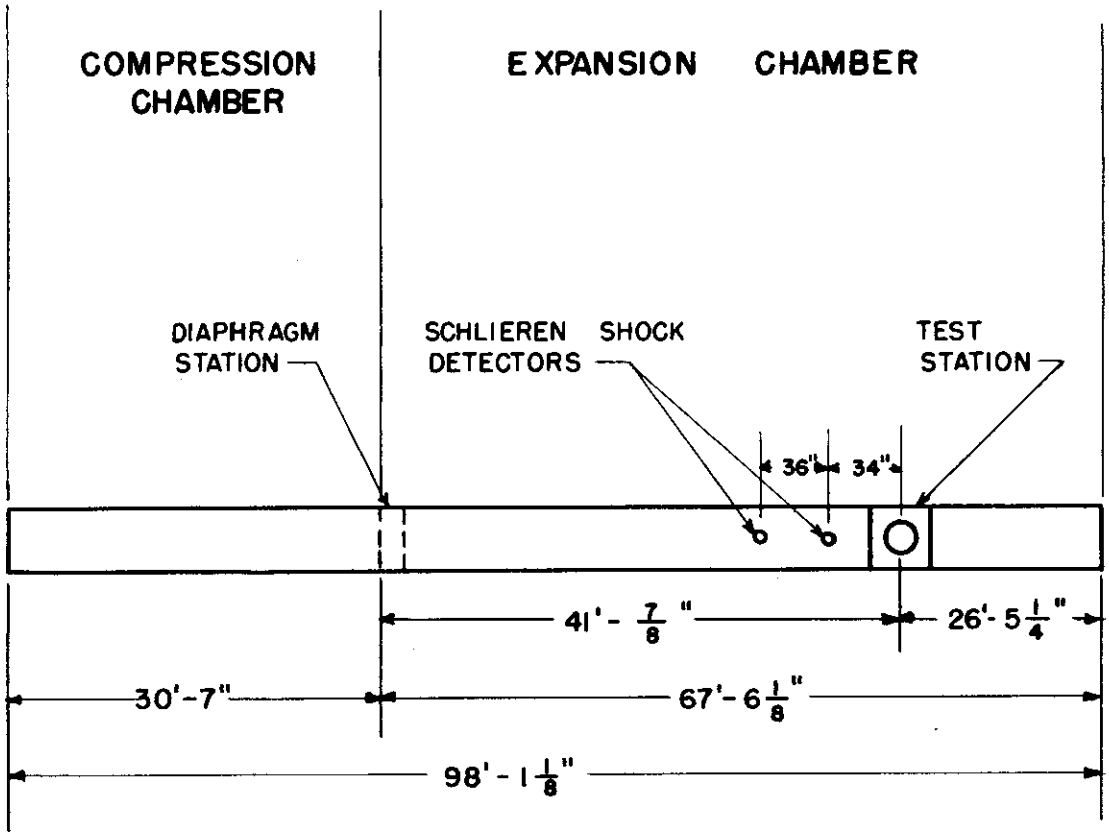

INTERNAL CROSS-SECTION	8" X 24"
INTERNAL LENGTH	98'- 1 1/8"
APPROXIMATE TOTAL WEIGHT OF SHOCK-TUBE PROPER	13 tons
MAXIMUM DESIGN PRESSURE	250 psia
MAXIMUM REYNOLD'S NO. WITH A 4-IN. CHORD MODEL AND AIR IN THE EXPANSION CHAMBER	6,750,000
MAXIMUM MACH NO. CURRENTLY OBTAINABLE WITH AIR IN THE EXPANSION CHAMBER	1.5

FIG. 4 SUMMARY OF PHYSICAL DATA ON THE MIT-WADC SHOCK-TUBE

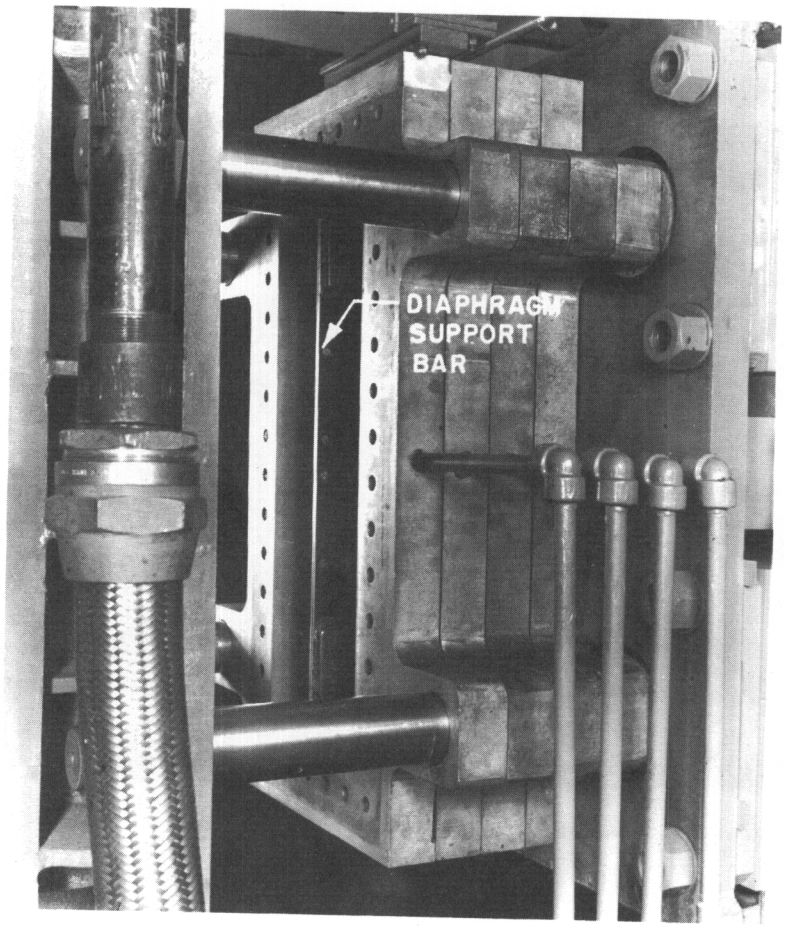

FIG. 5 SHOCK TUBE DIAPHRAGM SECTION

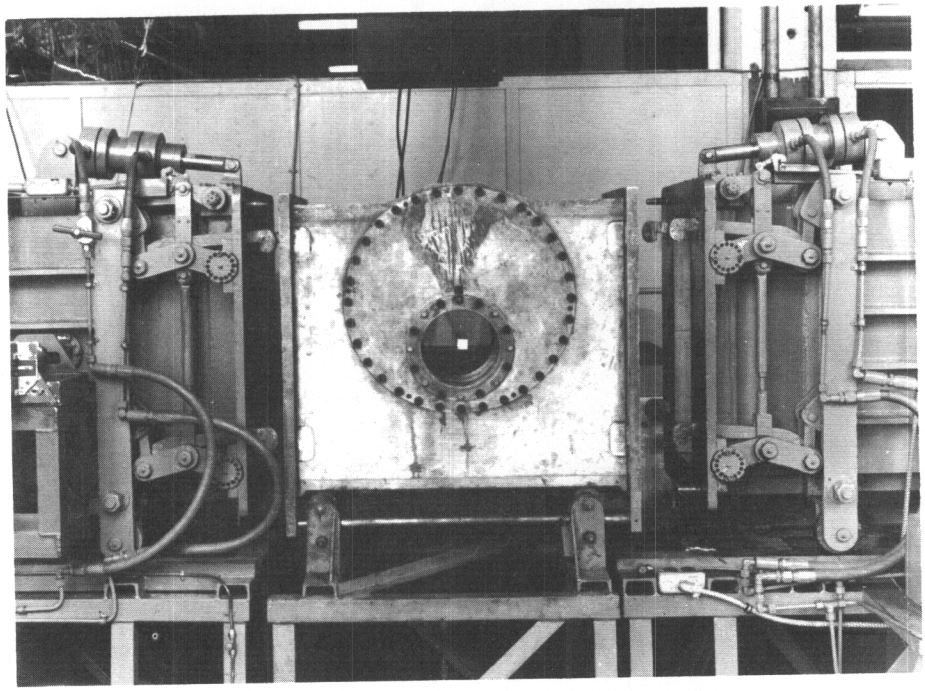

FIG. 6 SHOCK TUBE TEST SECTION

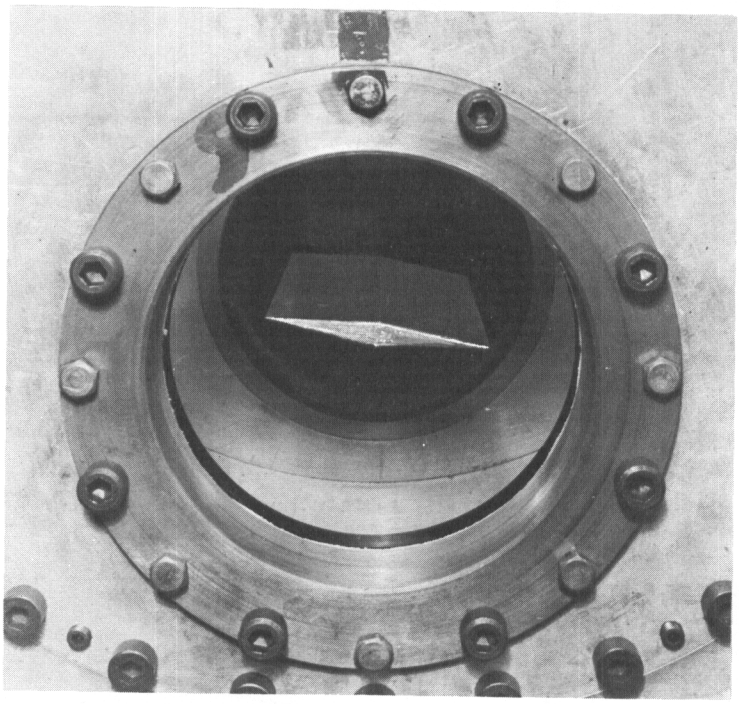

FIG. 7 DOUBLE-WEDGE AIRFOIL MOUNTED IN THE TEST SECTION

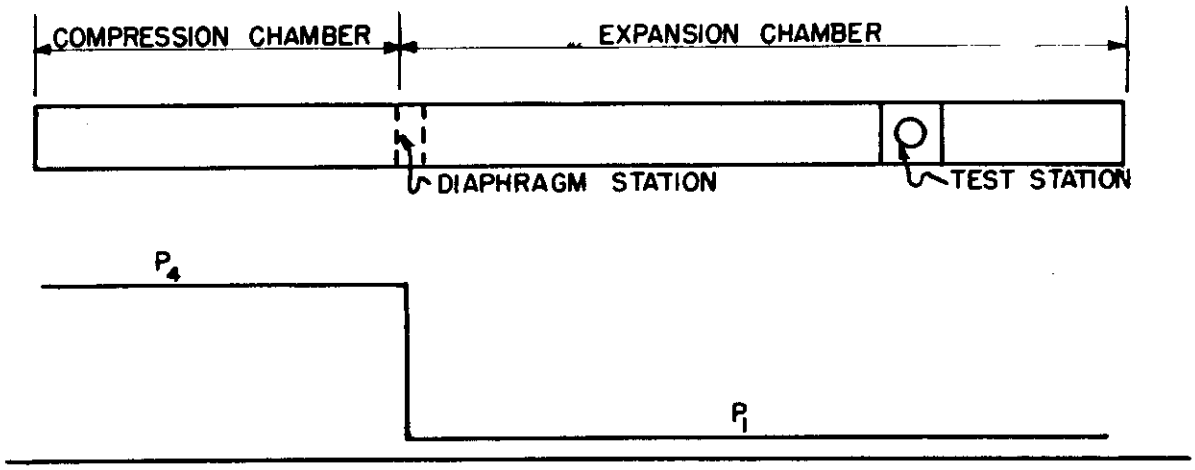

PRESSURE DISTRIBUTION IN TUBE BEFORE DIAPHRAGM BURST

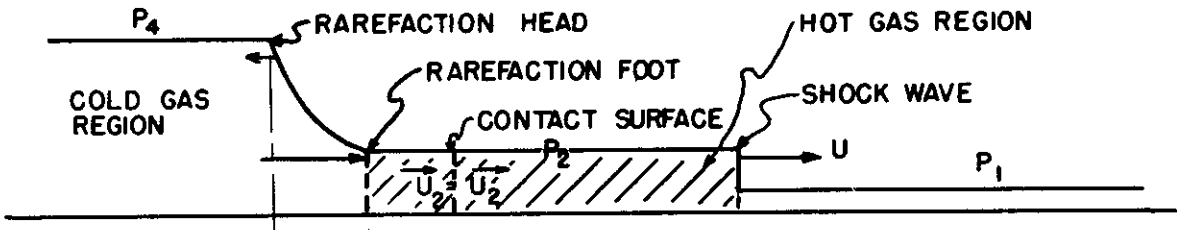

PRESSURE DISTRIBUTION IN TUBE SHORTLY AFTER DIAPHRAGM BURST

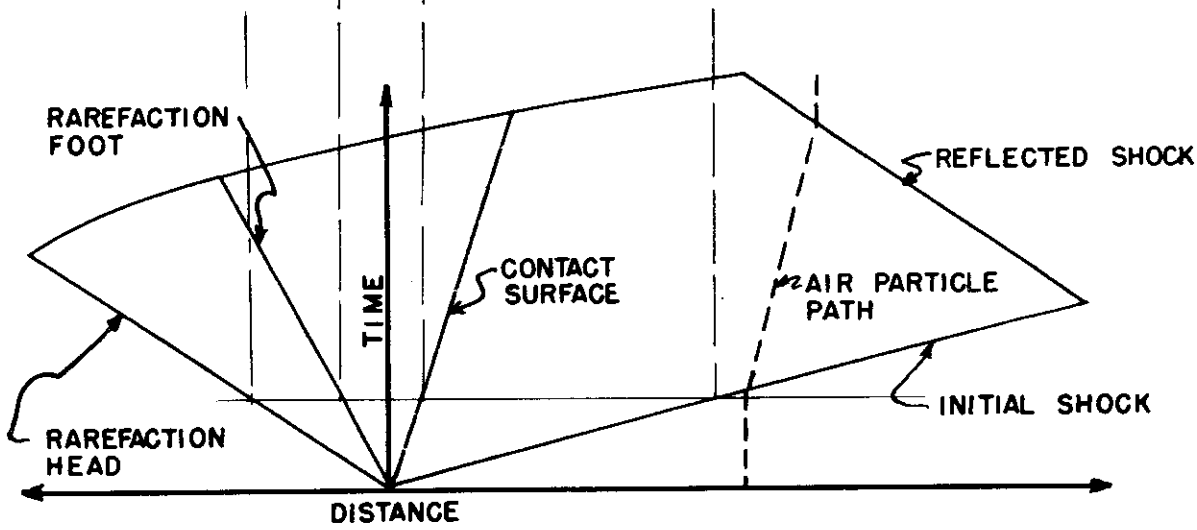

x-t DIAGRAM OF SHOCK TUBE FLOW AND WAVE PHENOMENA

FIG. 8 SCHEMATIC OF IDEAL SHOCK TUBE PRESSURE, FLOW, AND WAVE PHENOMENA

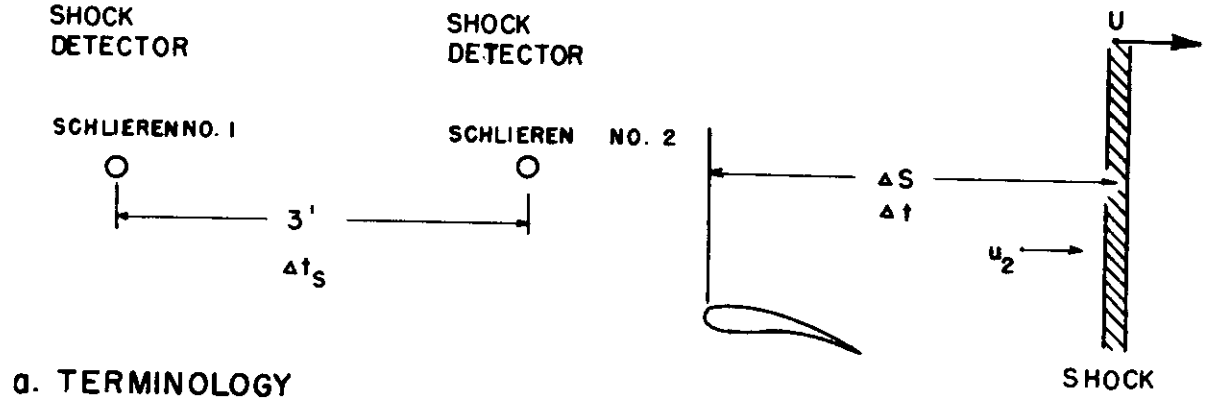

a. TERMINOLOGY

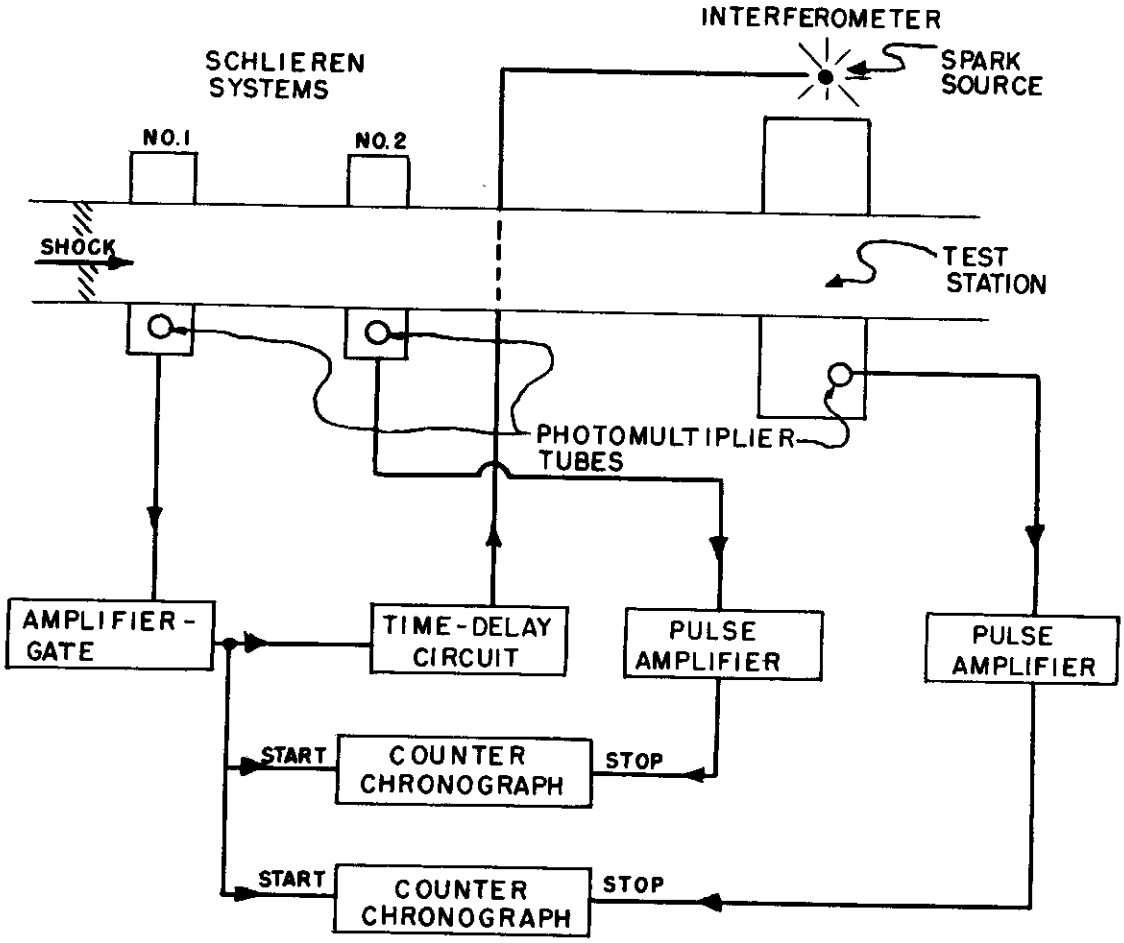

b. DIAGRAM OF ELECTRONIC COMPONENTS

FIG. 9 SCHEMATIC OF THE METHOD USED FOR MEASURING THE SPEED OF THE FLOW-INIATING SHOCK

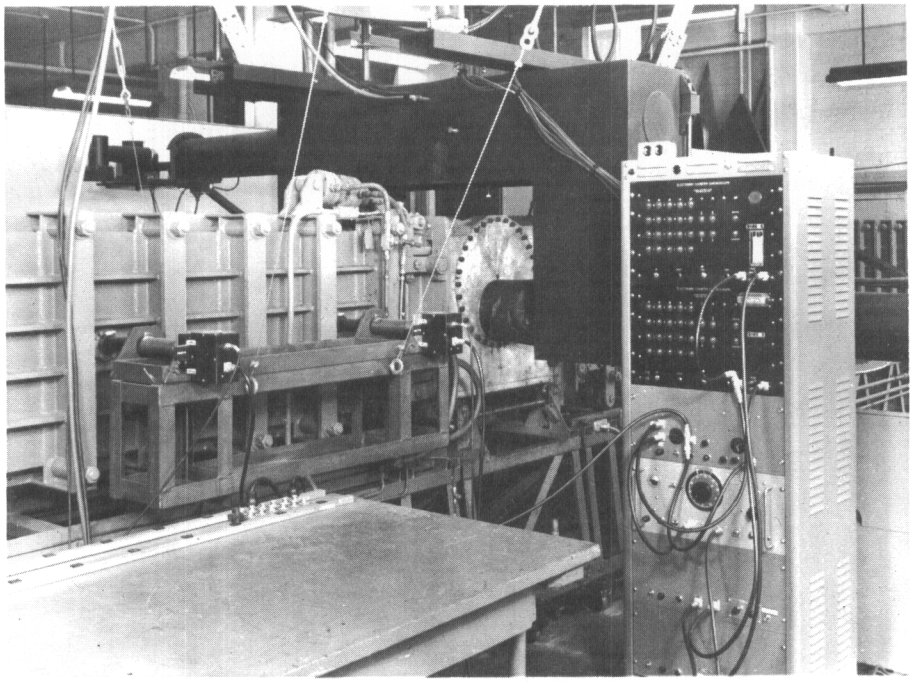

FIG. 10 VIEW OF THE INTERFEROMETER AND THE SHOCK-TIMING INSTRUMENTATION

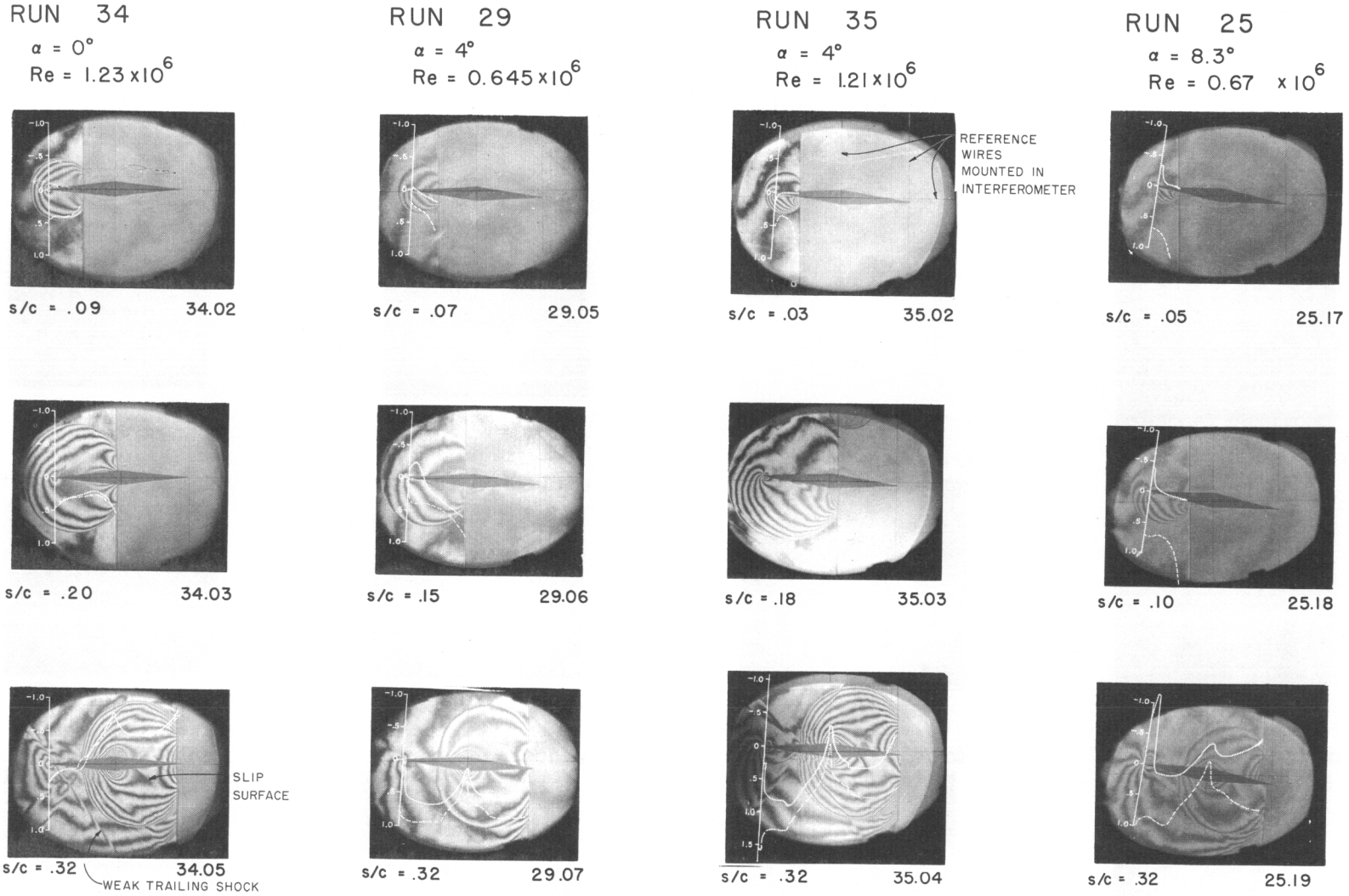

FIG. 11a SEQUENCE OF INFINITE-FRINGE FLOW INTERFEROGRAMS ILLUSTRATING AIRFLOW DEVELOPMENT AND DISTRIBUTION OF SURFACE PRESSURE COEFFICIENT AROUND THE AIRFOIL, M = 0.4

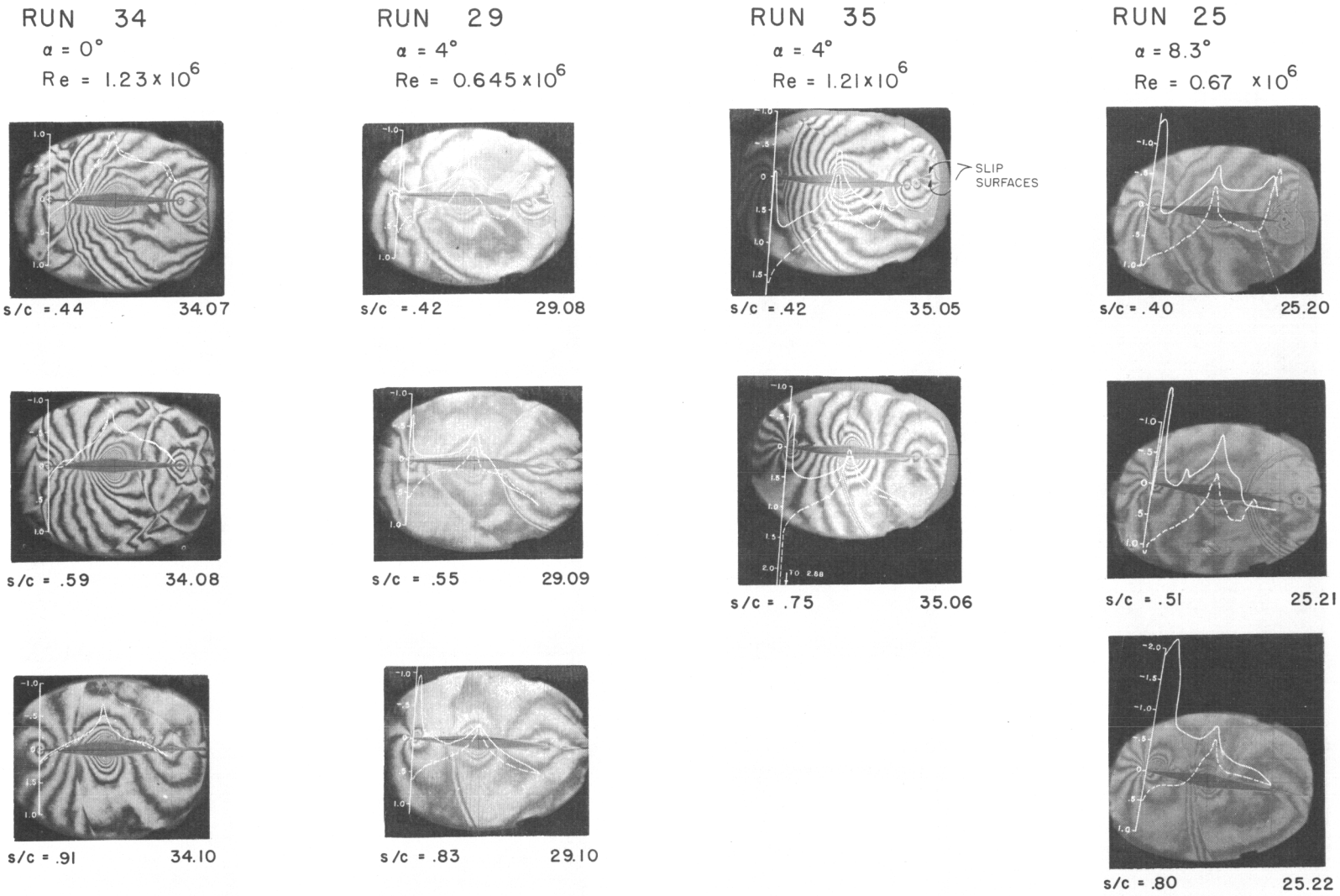

FIG. 11b SEQUENCE OF INFINITE-FRINGE FLOW INTERFEROGRAMS ILLUSTRATING AIRFLOW DEVELOPMENT AND DISTRIBUTION OF SURFACE PRESSURE COEFFICIENT AROUND THE AIRFOIL, M = 0.4

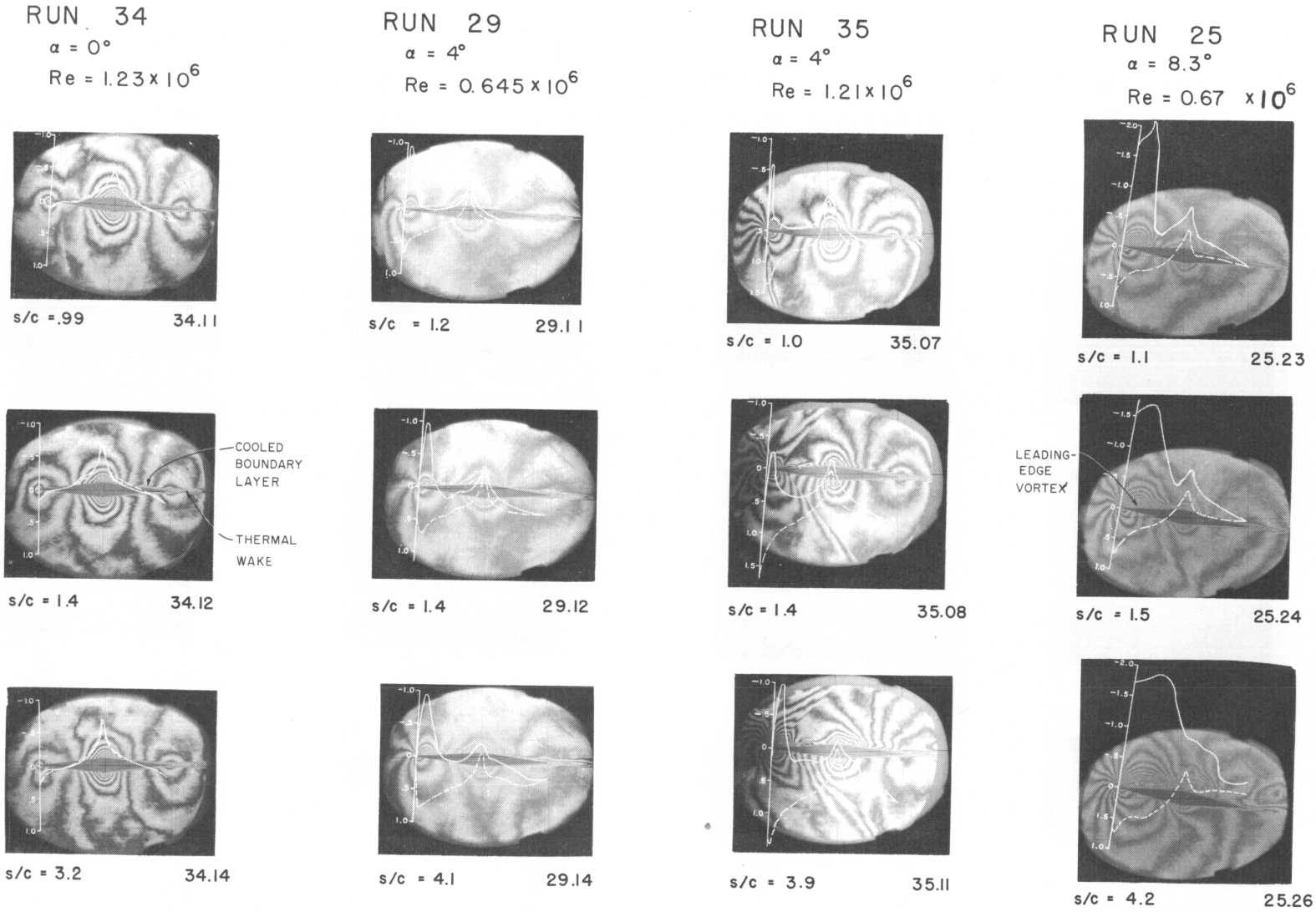

FIG. 11c SEQUENCE OF INFINITE-FRINGE FLOW INTERFEROGRAMS ILLUSTRATING AIRFLOW DEVELOPMENT AND DISTRIBUTION OF SURFACE PRESSURE COEFFICIENT AROUND THE AIRFOIL, M= 0.4

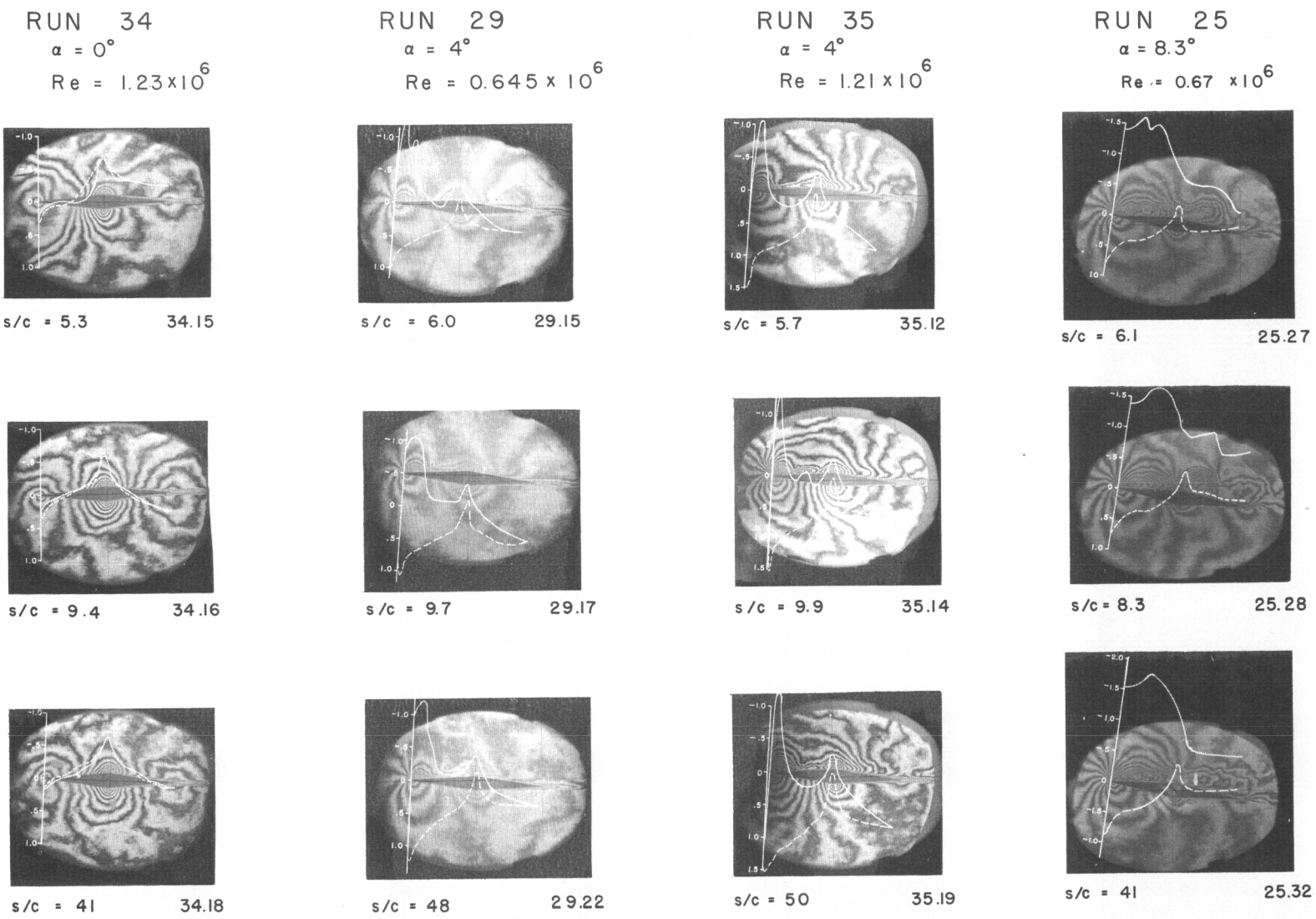

FIG. IId SEQUENCE OF INFINITE-FRINGE FLOW INTERFEROGRAMS ILLUSTRATING AIRFLOW DEVELOPMENT AND DISTRIBUTION OF SURFACE PRESSURE COEFFICIENT AROUND THE AIRFOIL, M = 0.4

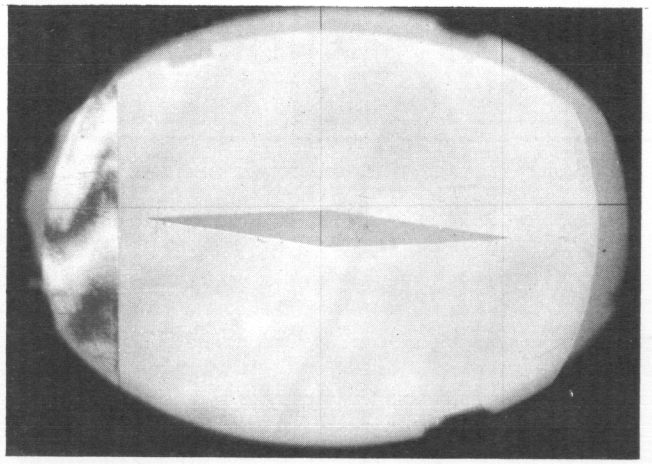

a. INFINITE FRINGE

NO FLOW

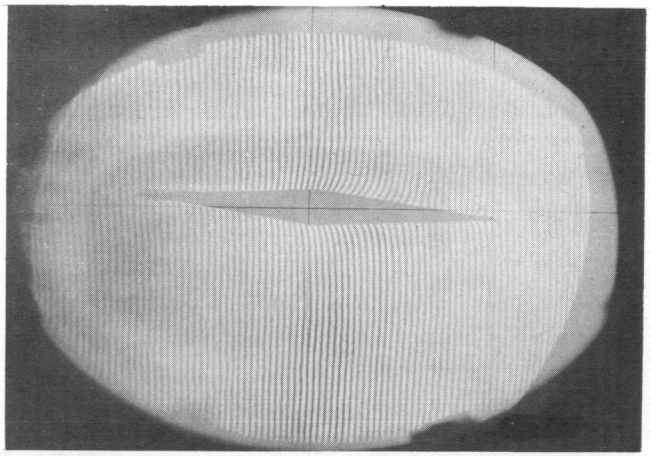

c. FINITE FRINGE

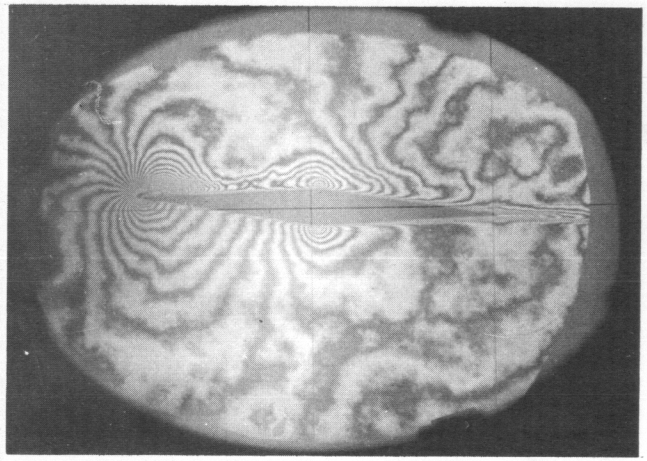

b. INFINITE FRINGE

WITH FLOW

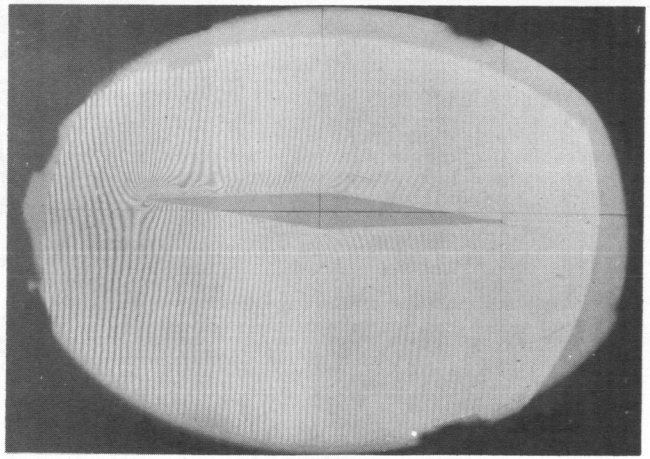

d. FINITE FRINGE

FIG. 12 TYPICAL INTERFEROGRAMS WITH AND WITHOUT FLOW

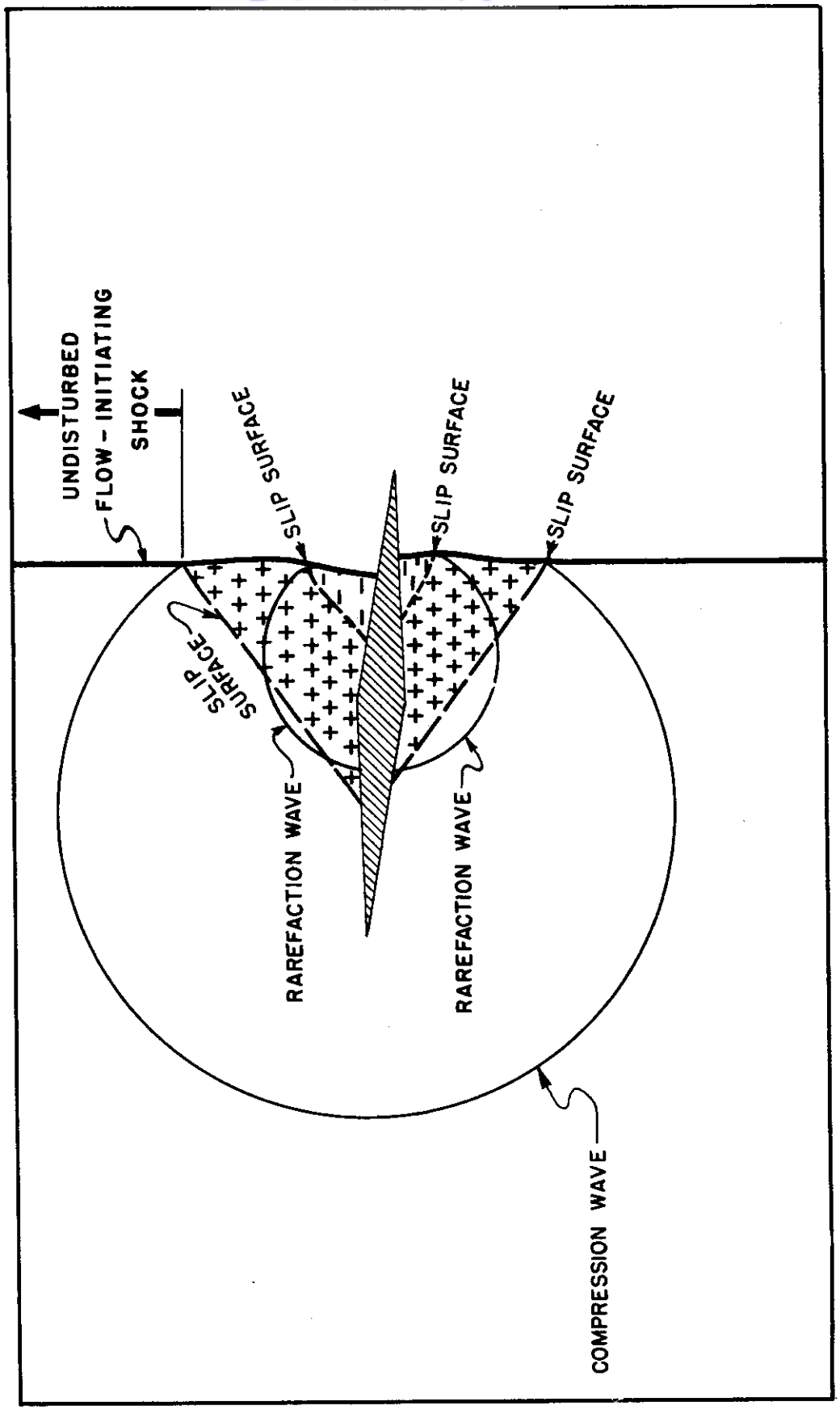

FIG. 13 SCHEMATIC ENTROPY DISTRIBUTION ABOUT THE AIRFOIL AT $\alpha = 4°$

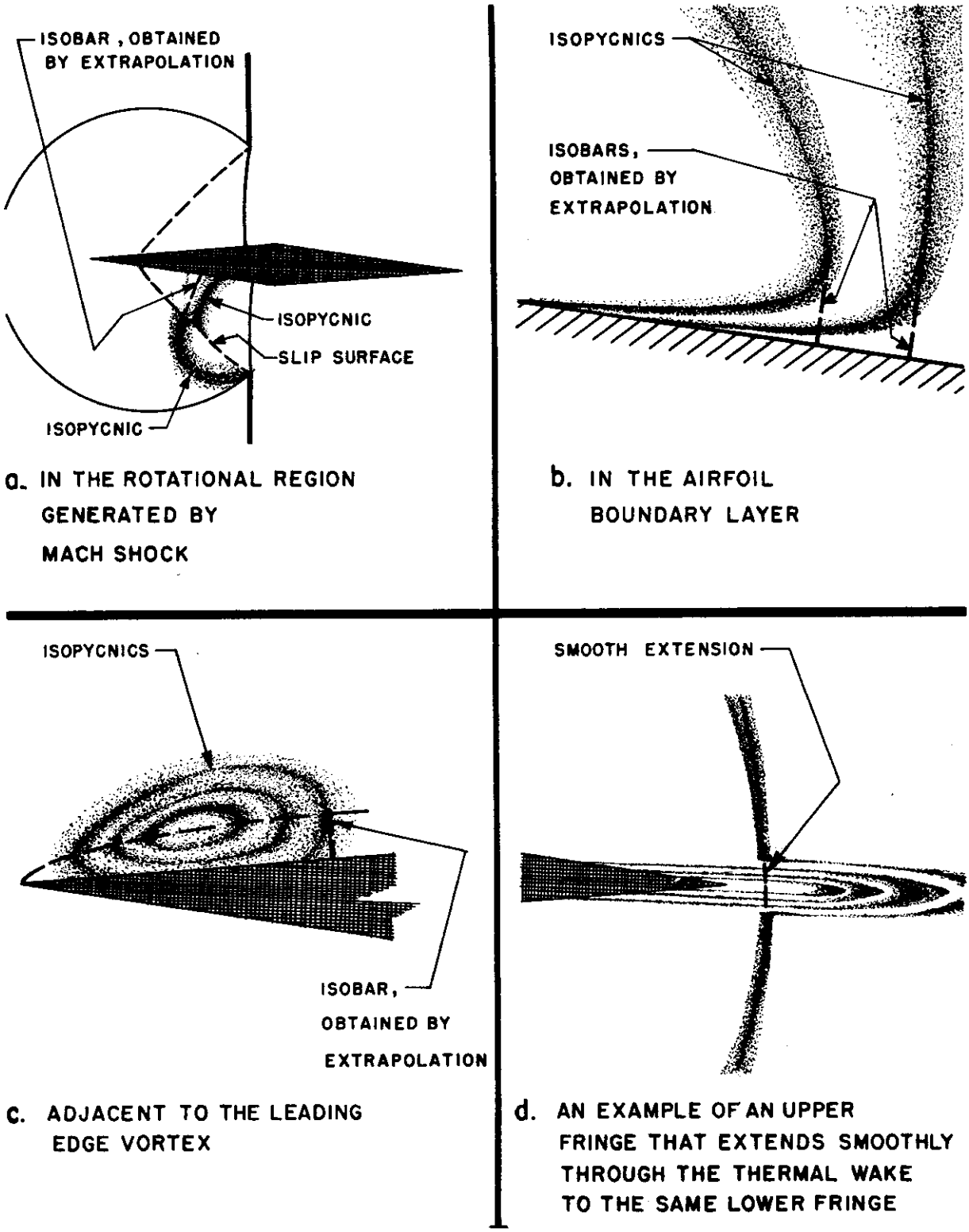

FIG. 14 DIAGRAMS TO ILLUSTRATE THE METHOD OF DETERMINING THE SURFACE PRESSURE FROM THE INTERFEROGRAM FRINGES

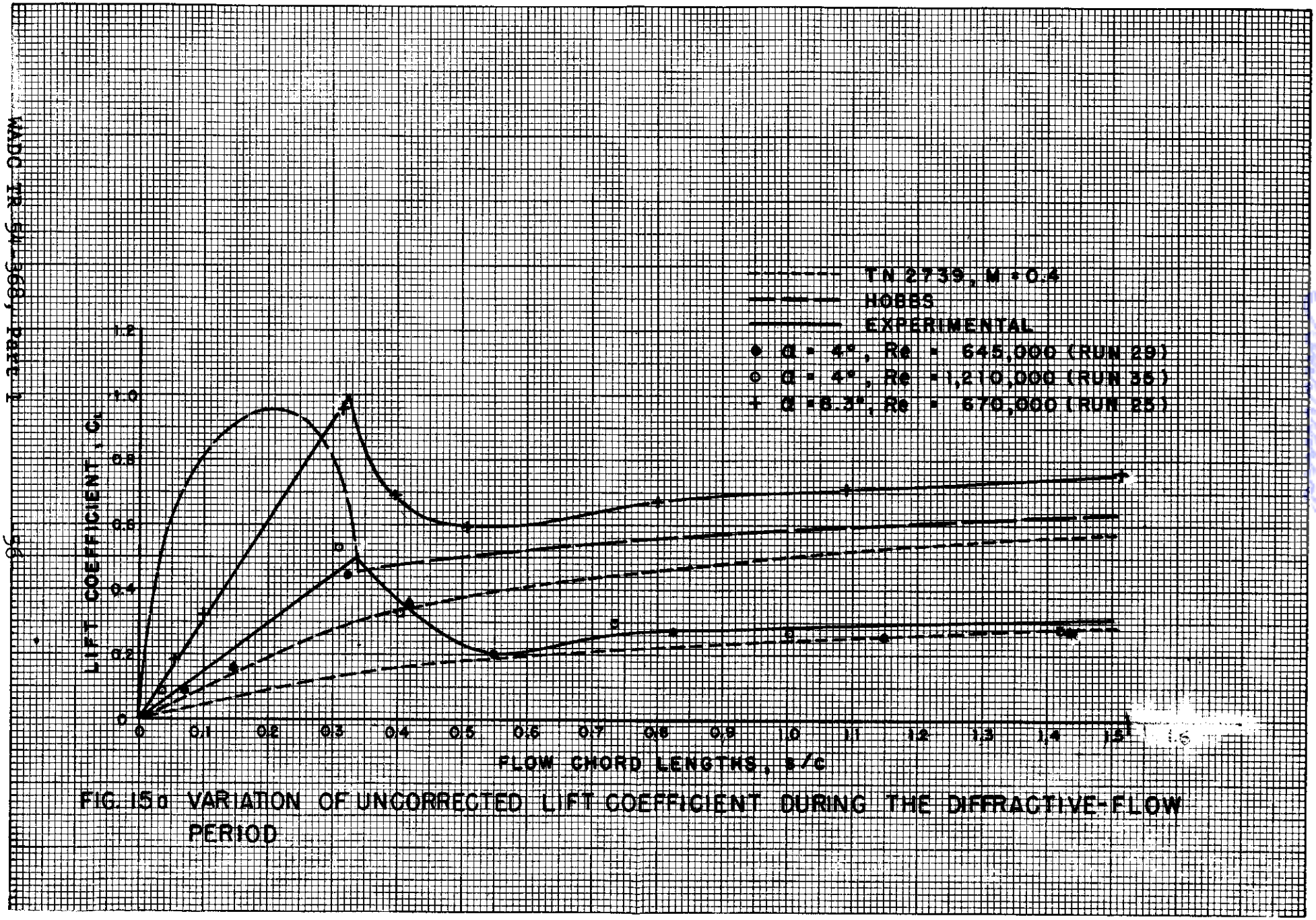

FIG. 15a VARIATION OF UNCORRECTED LIFT COEFFICIENT DURING THE DIFFRACTIVE-FLOW PERIOD

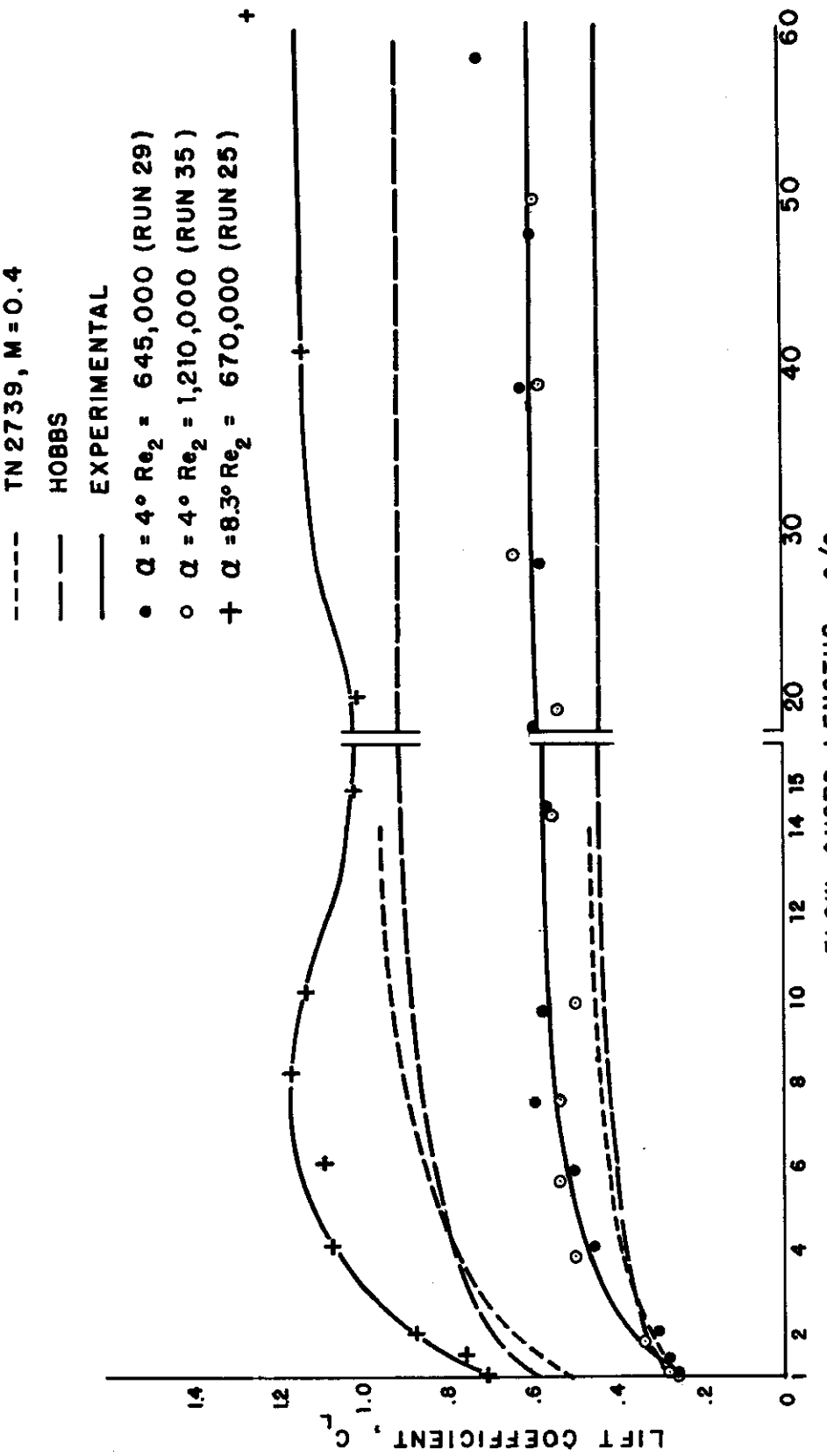

FIG. 15b VARIATION OF UNCORRECTED LIFT COEFFICIENT DURING THE POST-DIFFRACTIVE FLOW PERIOD

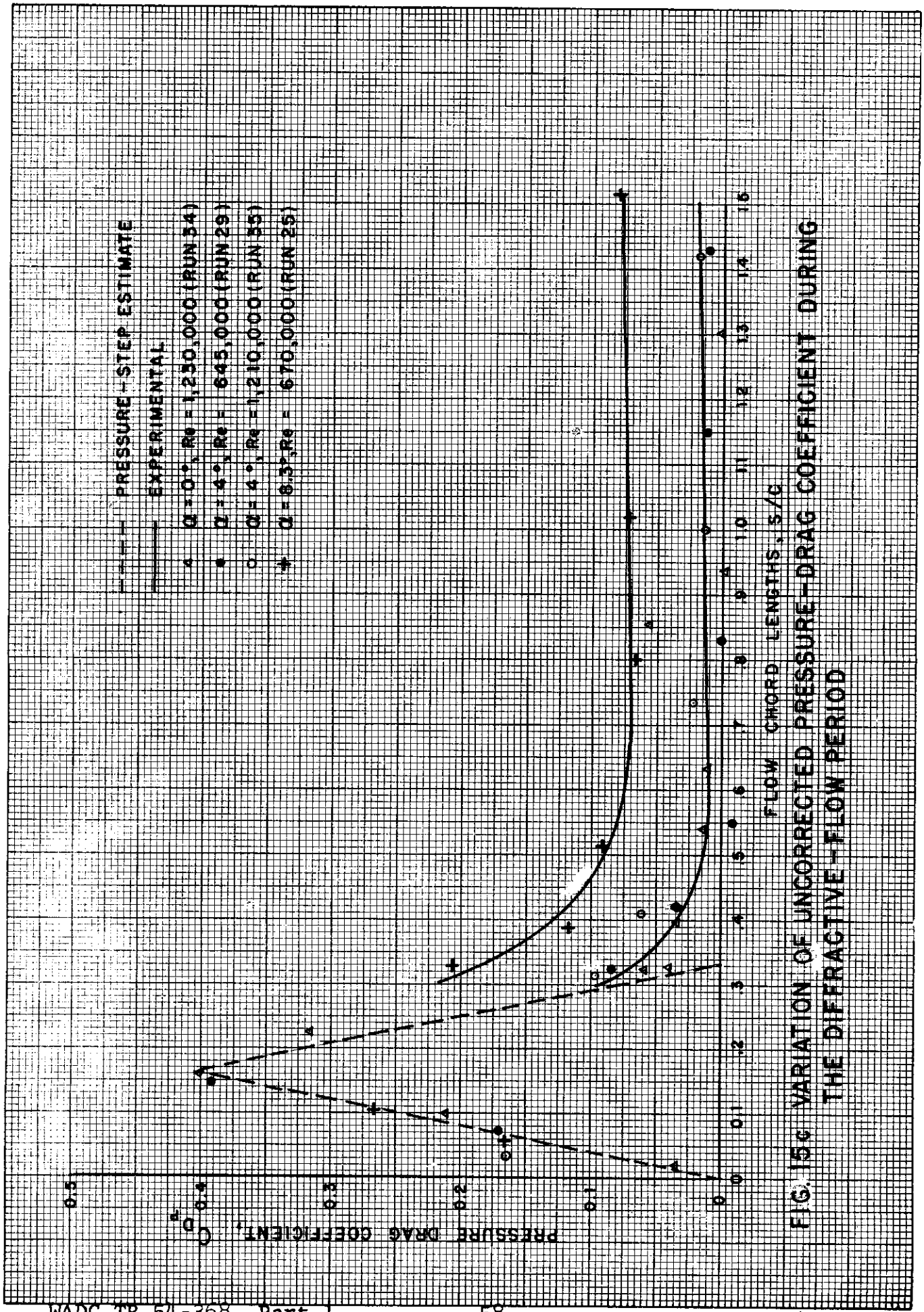

FIG. 15c VARIATION OF UNCORRECTED PRESSURE-DRAG COEFFICIENT DURING THE DIFFRACTIVE-FLOW PERIOD

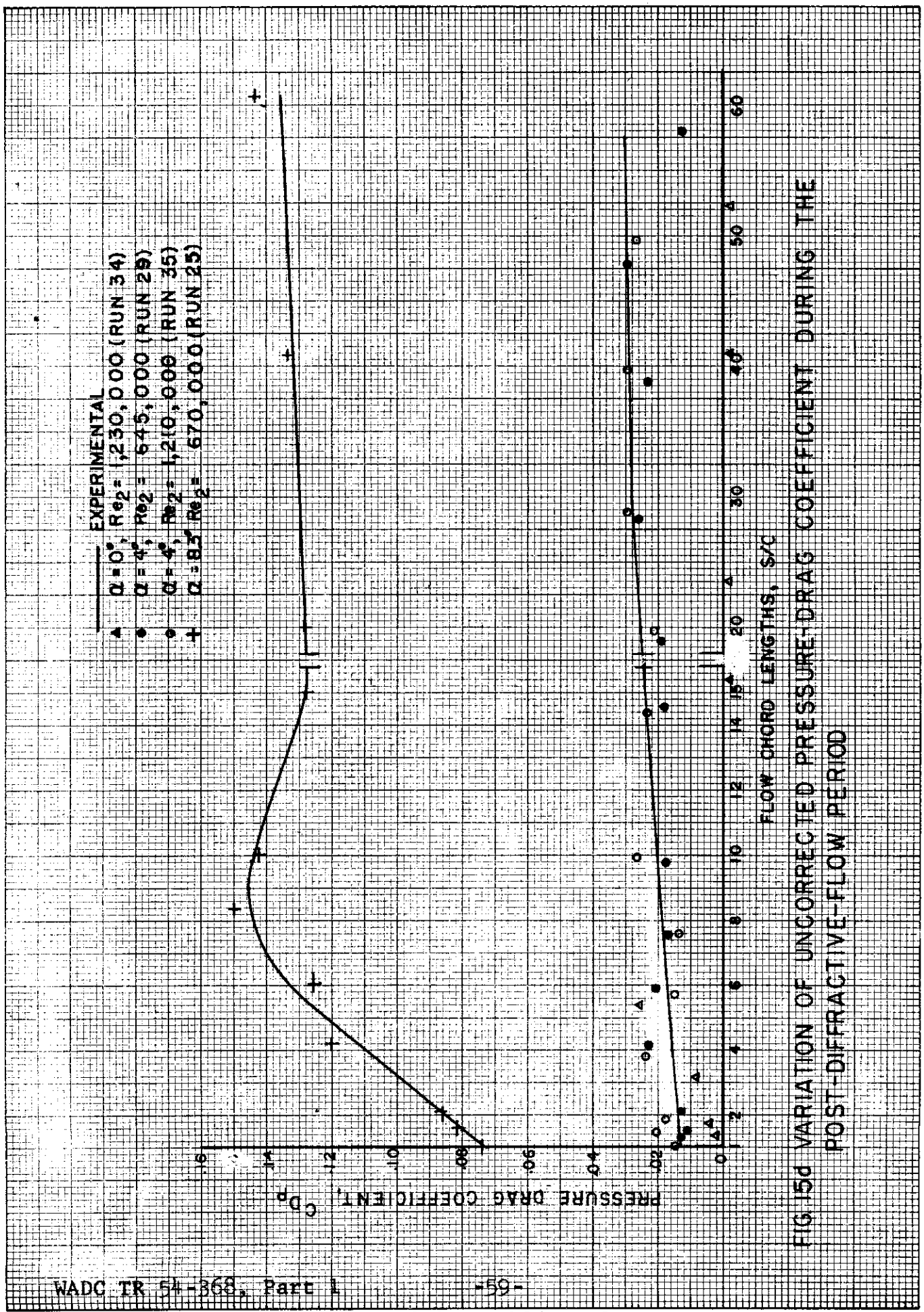

FIG. 15d VARIATION OF UNCORRECTED PRESSURE-DRAG COEFFICIENT DURING THE POST-DIFFRACTIVE-FLOW PERIOD

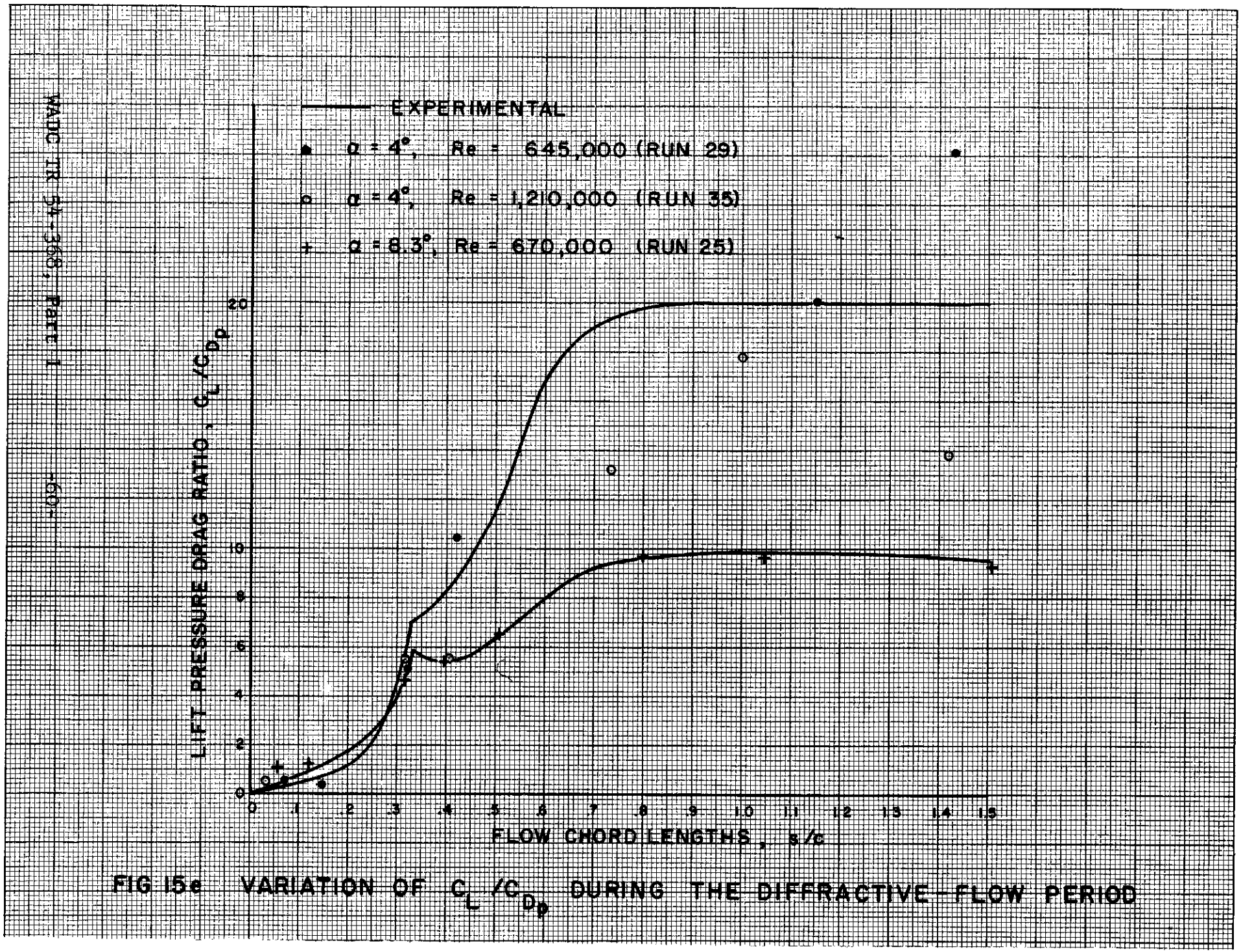

FIG 15e VARIATION OF C_L/C_{D_p} DURING THE DIFFRACTIVE-FLOW PERIOD

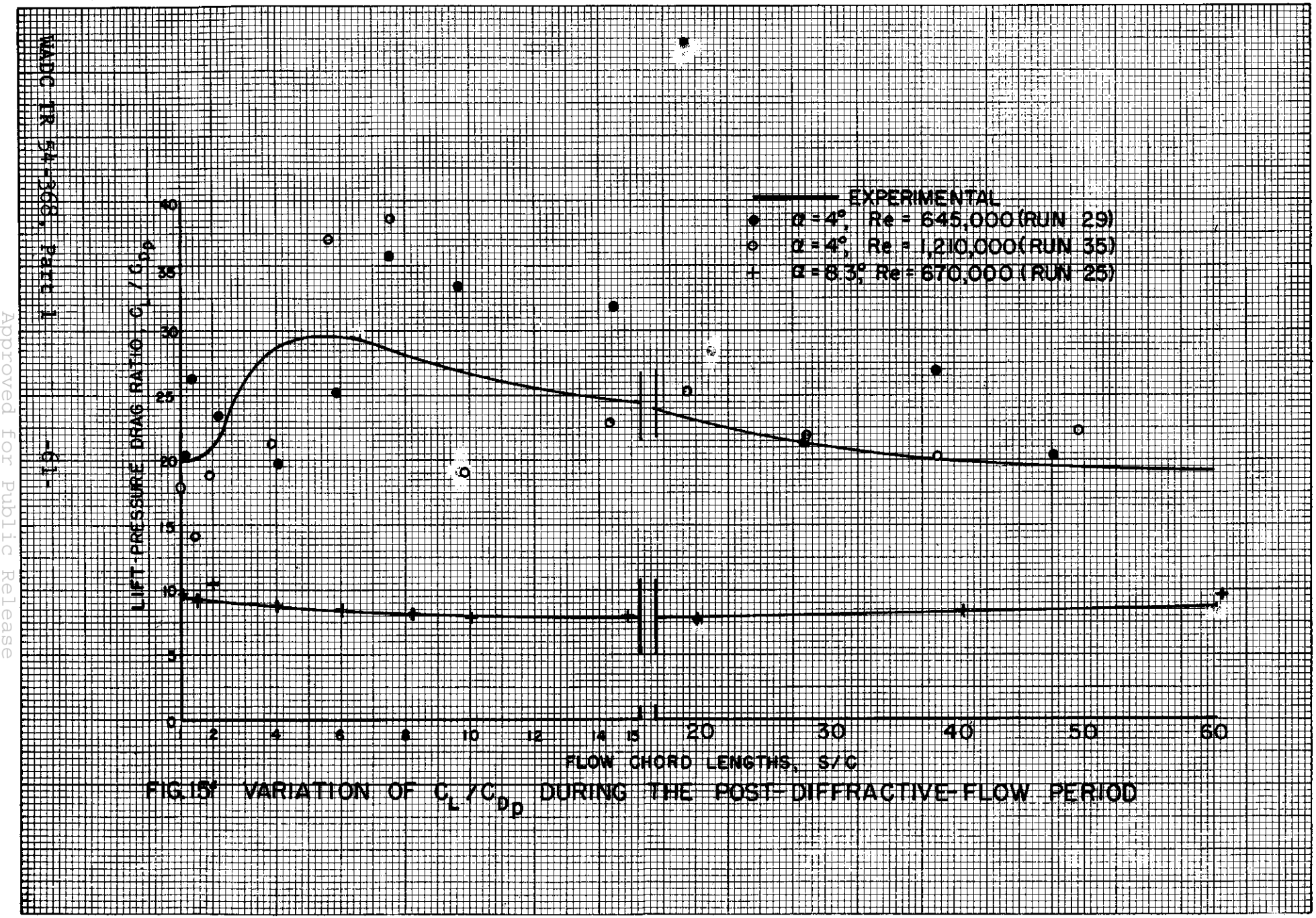

FIG. 15 VARIATION OF C_L/C_{D_p} DURING THE POST-DIFFRACTIVE-FLOW PERIOD

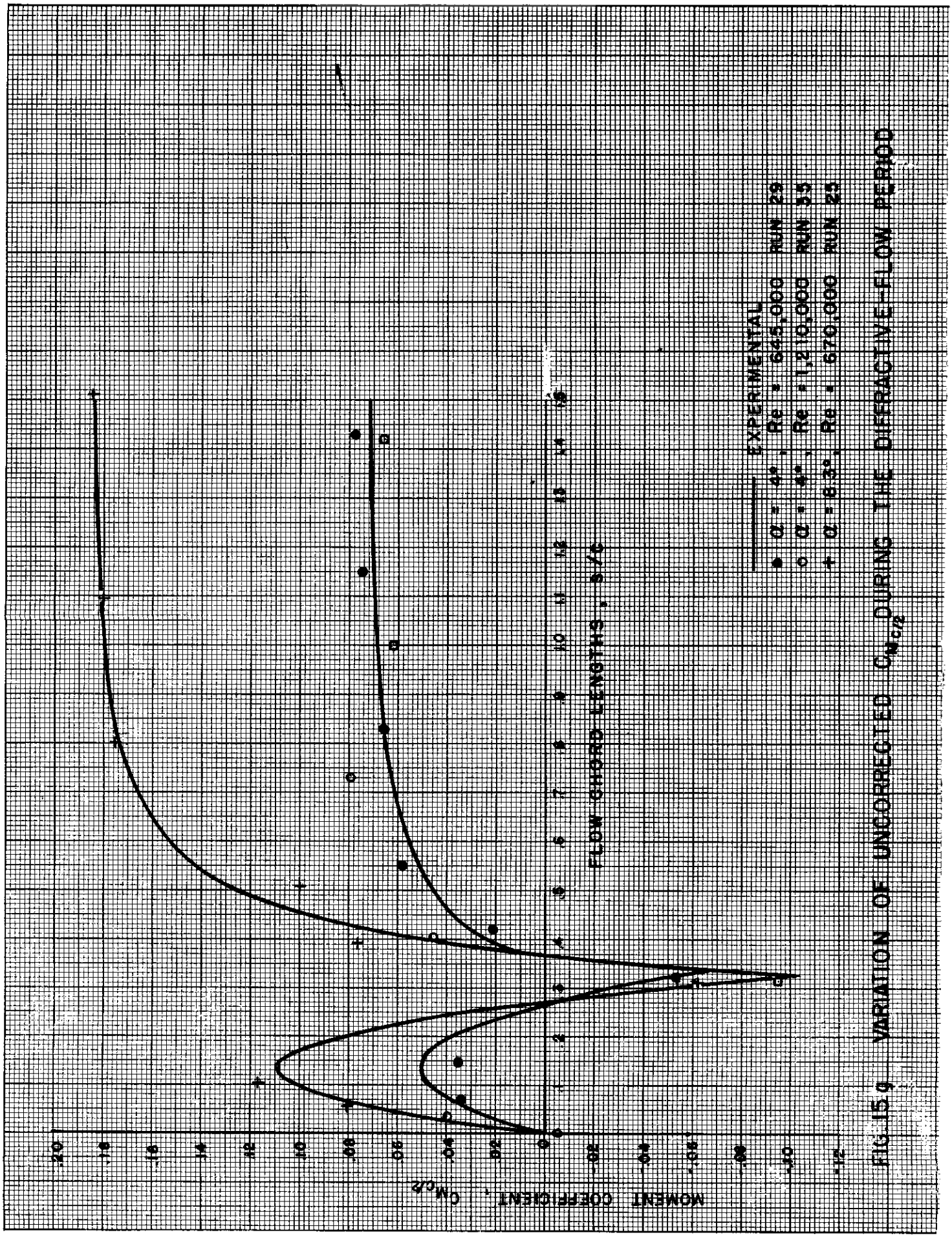

FIG. 15 a VARIATION OF UNCORRECTED $C_{M_{c/2}}$ DURING THE DIFFRACTIVE-FLOW PERIOD

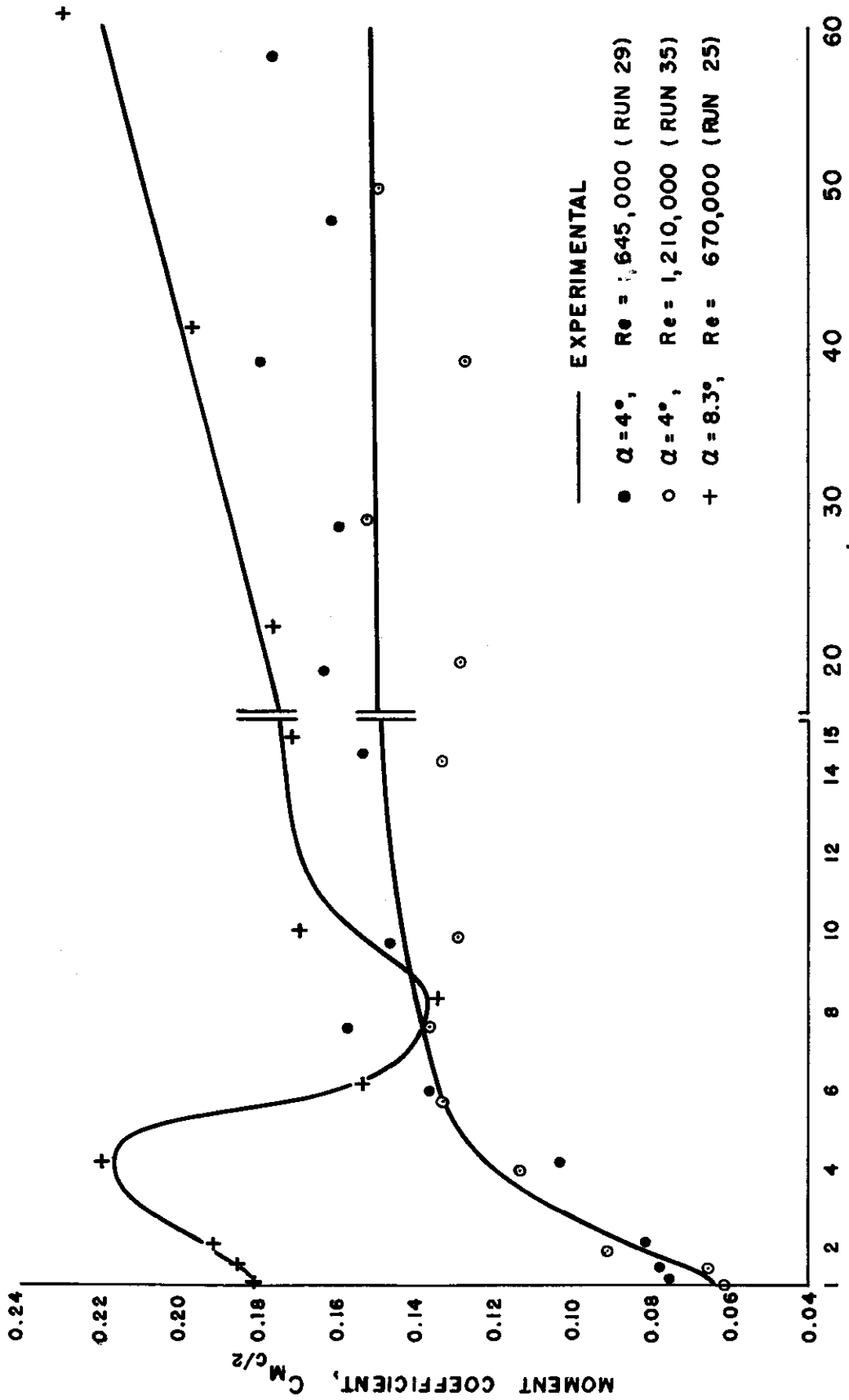

FIG. 15h VARIATION OF UNCORRECTED $C_{M_{c/2}}$ DURING THE POST-DIFFRACTIVE-FLOW PERIOD

FIG 15: VARIATION OF THE CENTER OF PRESSURE, MEASURED FROM THE LEADING EDGE, DURING THE DIFFRACTIVE-FLOW PERIOD

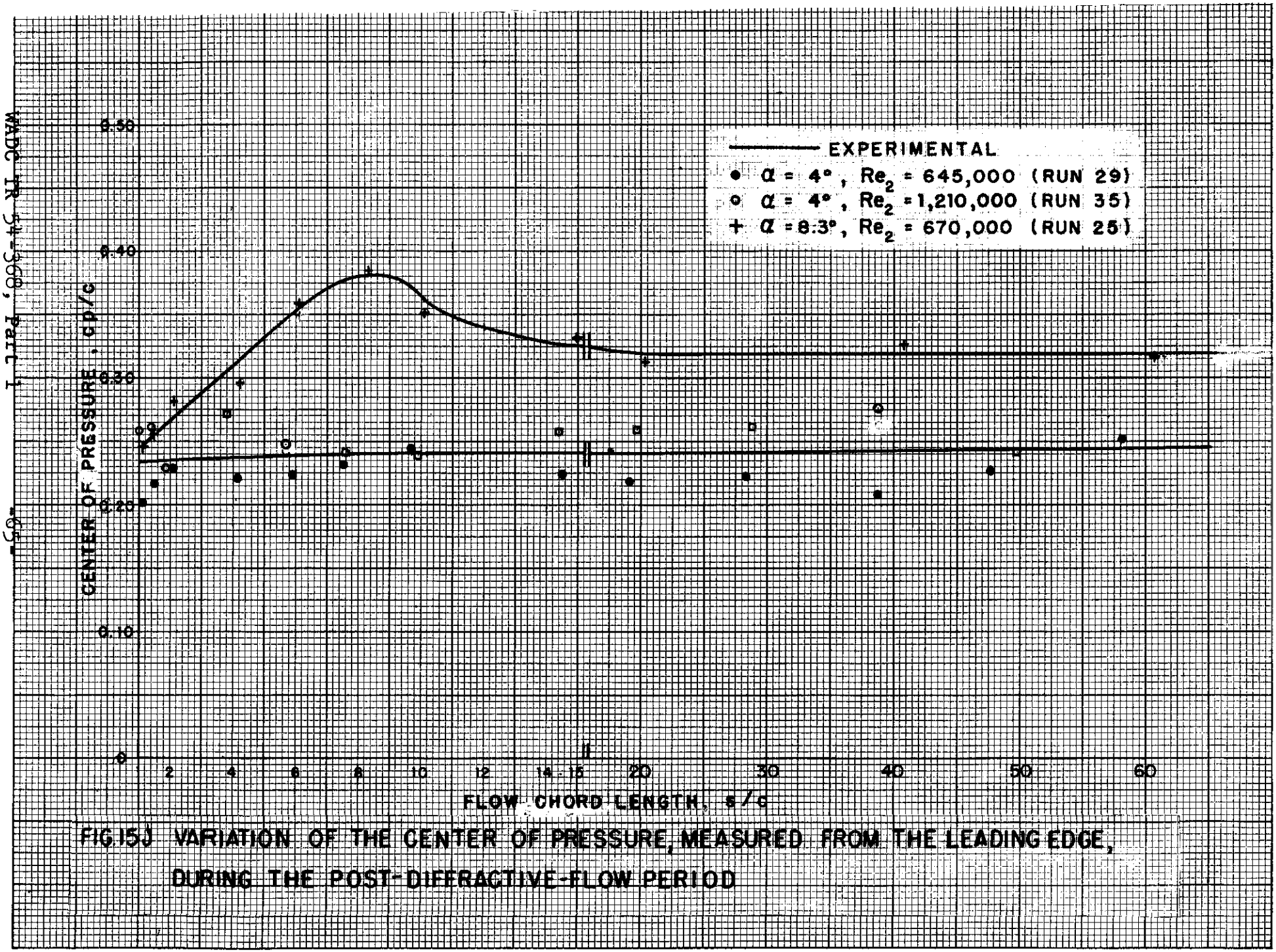

FIG 15J VARIATION OF THE CENTER OF PRESSURE, MEASURED FROM THE LEADING EDGE, DURING THE POST-DIFFRACTIVE-FLOW PERIOD

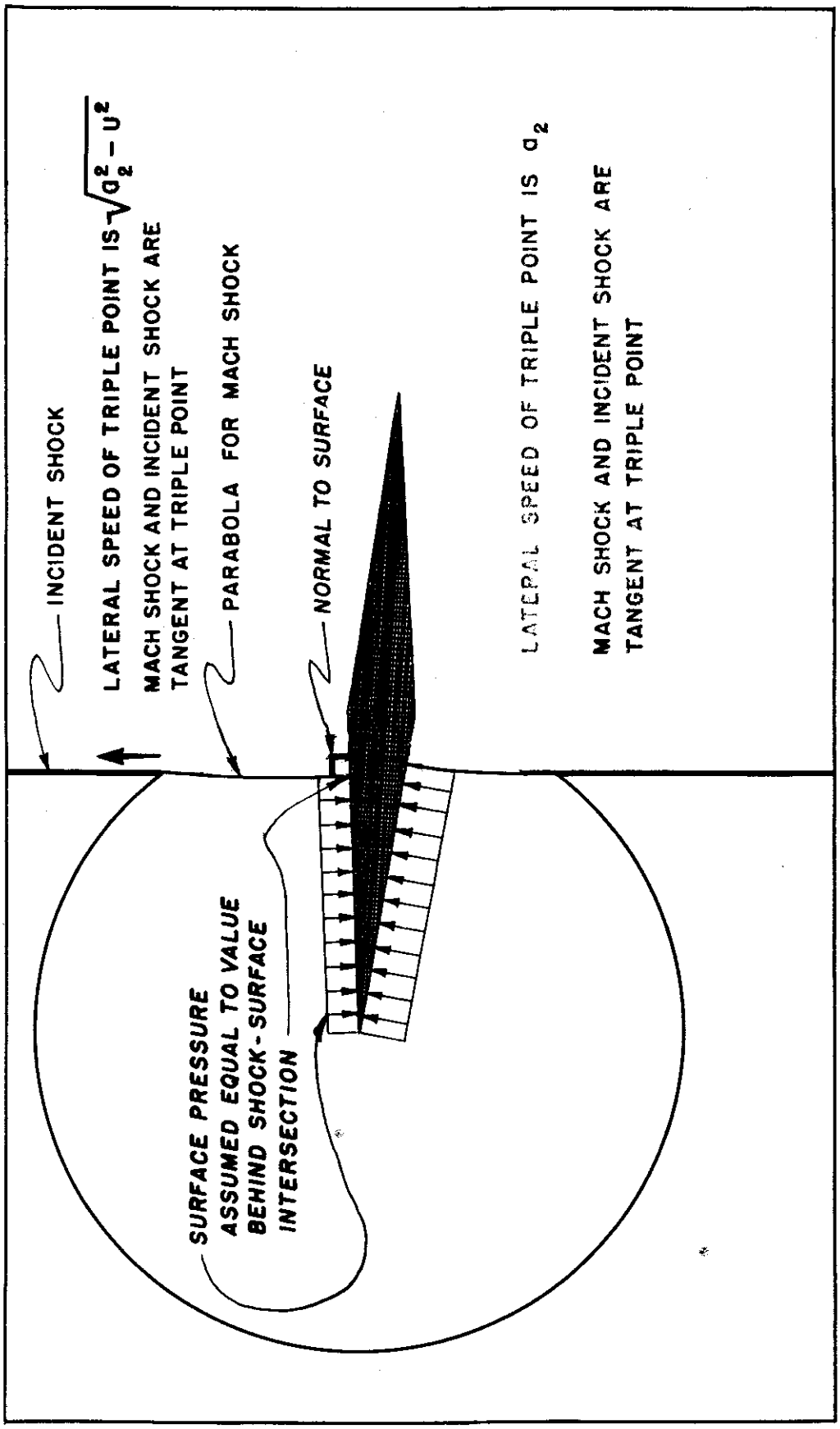

FIG. 16 SCHEMATIC OF SIMPLIFIED PARABOLIC-MACH-SHOCK MODEL

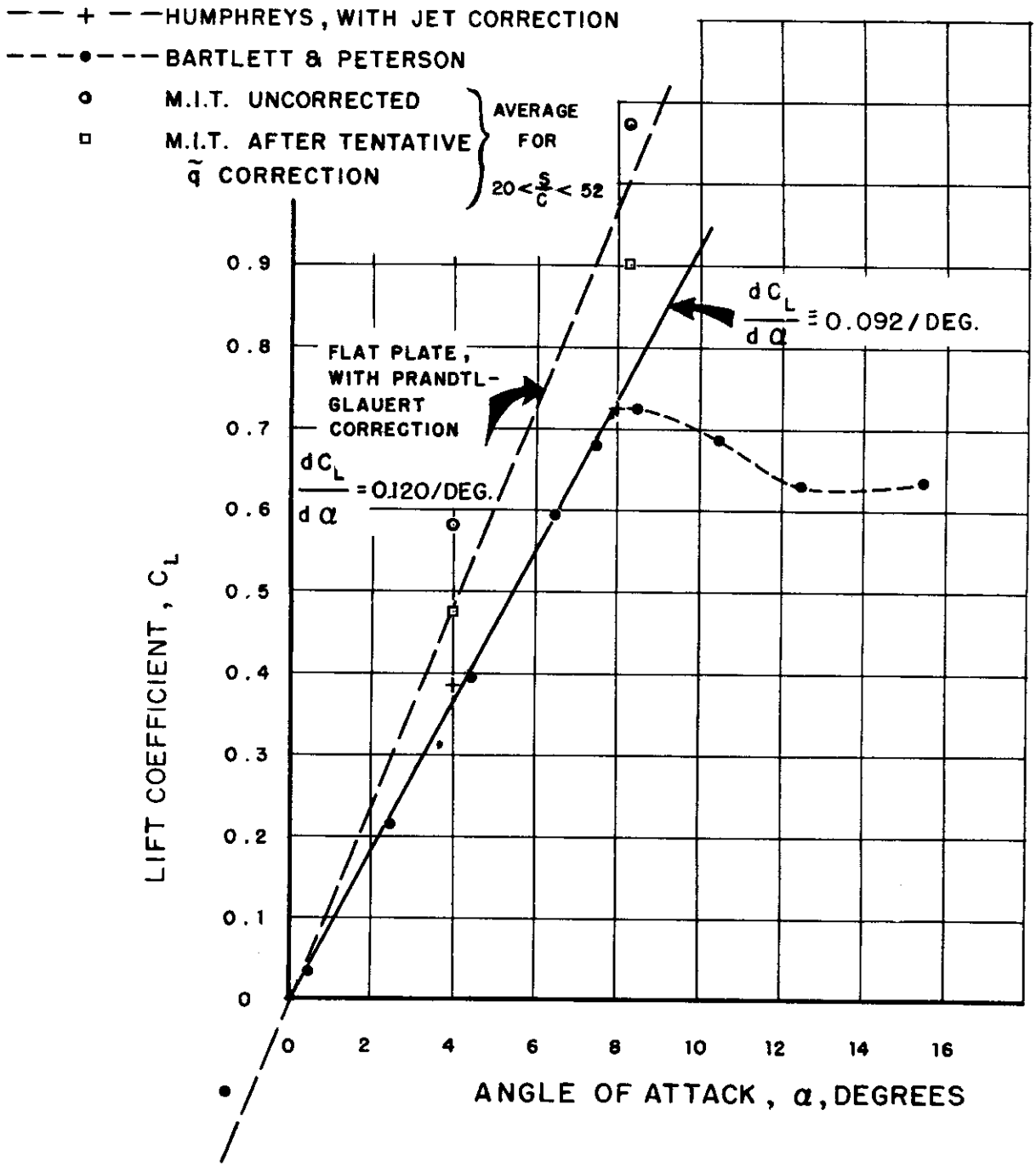

FIG. 17a COMPARISON OF STEADY-STATE LIFT COEFFICIENT VERSUS ANGLE OF ATTACK, M = 0.4

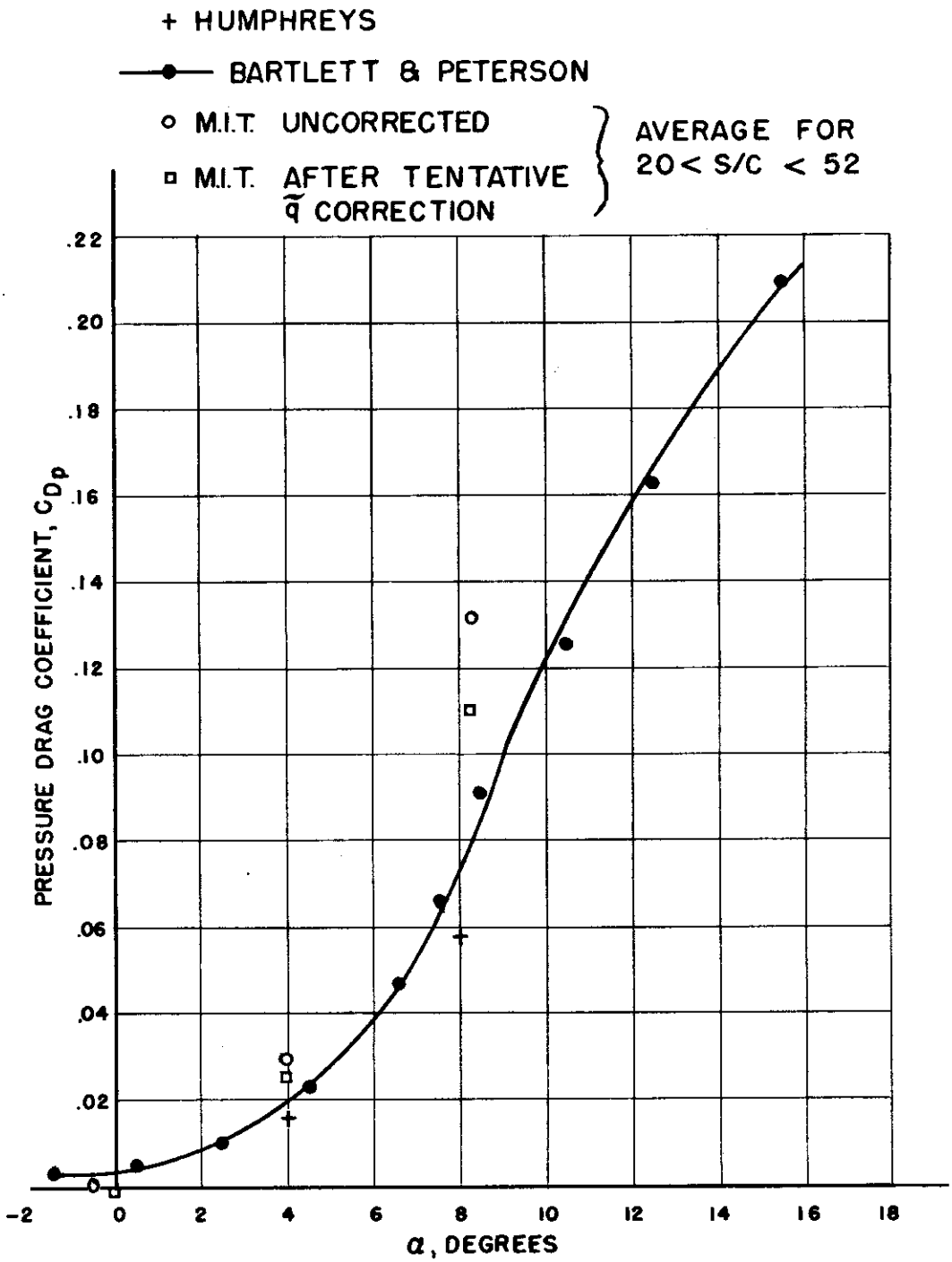

FIG. 17b COMPARISON OF STEADY-STATE PRESSURE DRAG COEFFICIENT VERSUS ANGLE OF ATTACK, M = 0.4

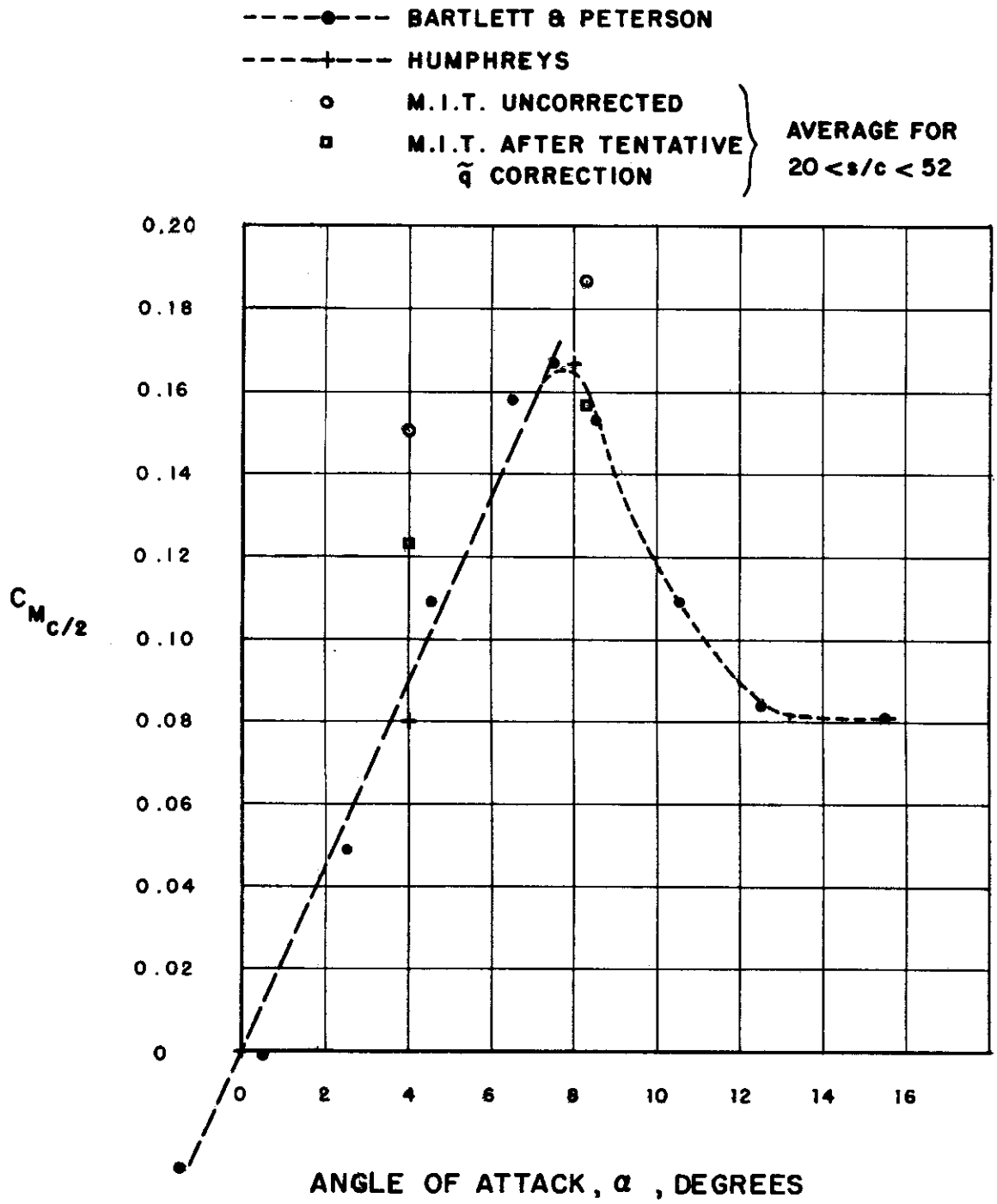

FIG. 17c COMPARISON OF STEADY-STATE VALUES OF $C_{M_{c/2}}$ VERSUS ANGLE OF ATTACK, M = 0.4

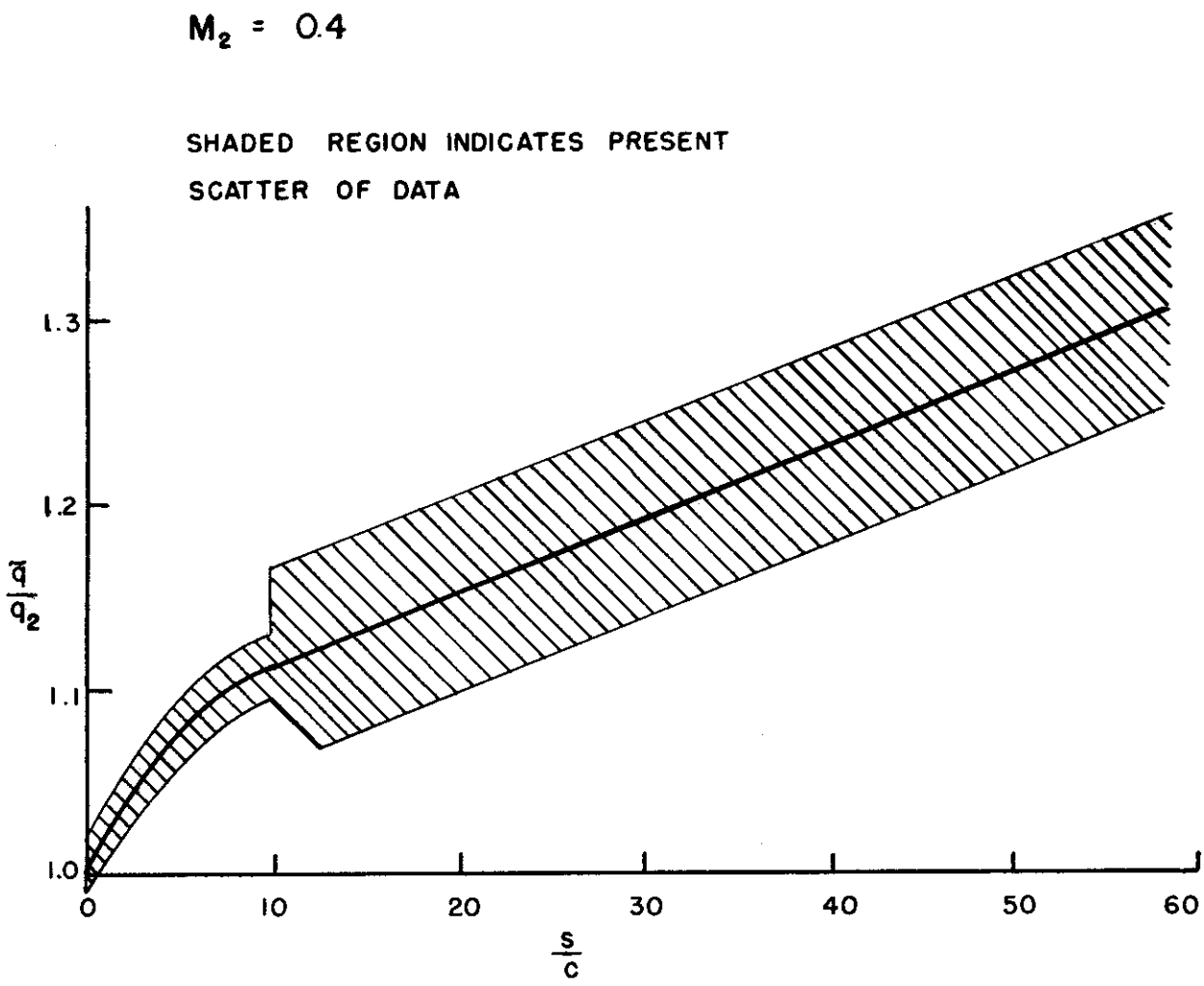

FIG. 18 TENTATIVE ESTIMATE OF THE FREE-STREAM DYNAMIC PRESSURE IN THE FLOW FOLLOWING THE FLOW-INITIATING SHOCK, AS INDICATED BY DENSITY-TIME MEASUREMENTS

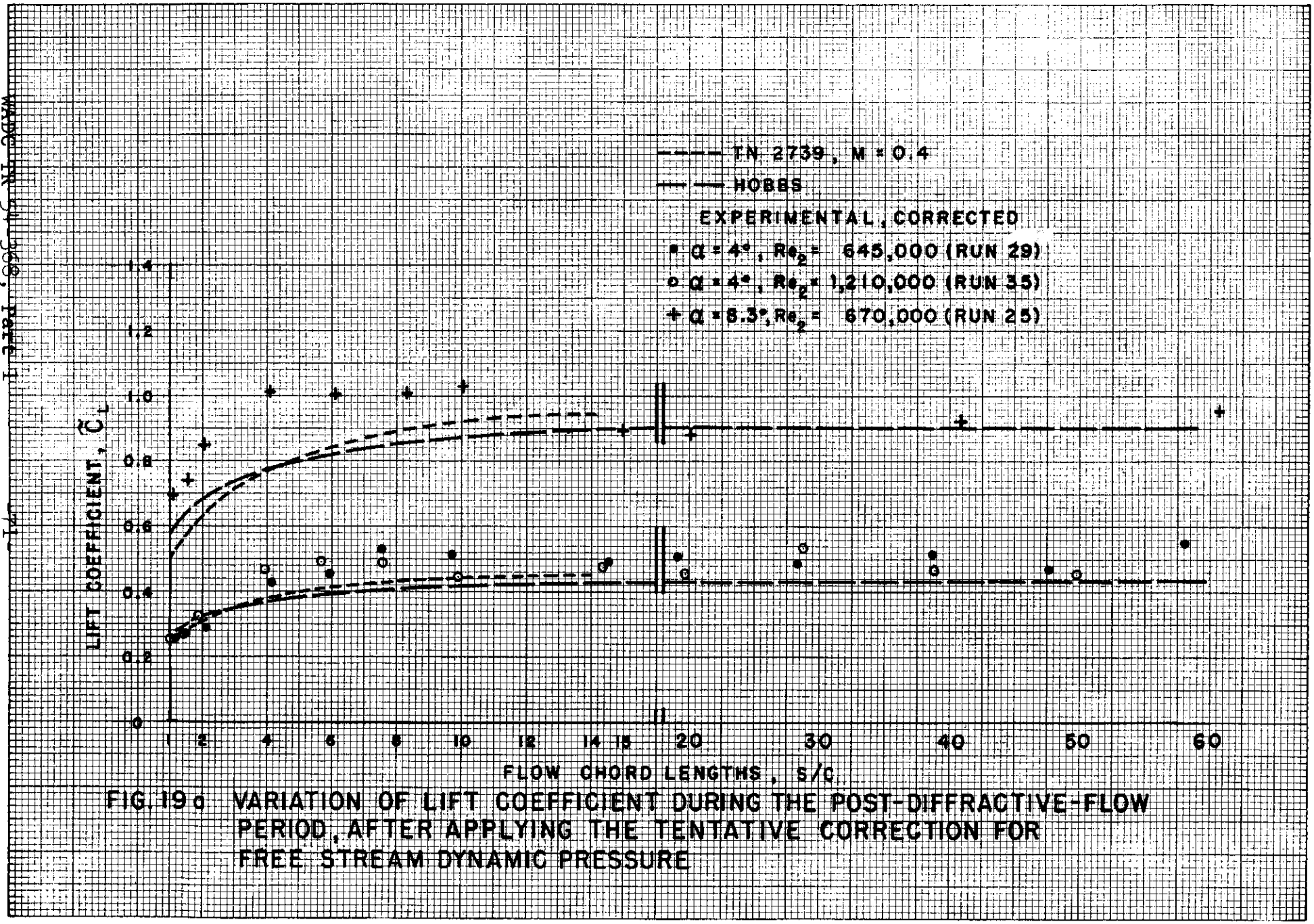

FIG. 19 c VARIATION OF LIFT COEFFICIENT DURING THE POST-DIFFRACTIVE-FLOW PERIOD, AFTER APPLYING THE TENTATIVE CORRECTION FOR FREE STREAM DYNAMIC PRESSURE

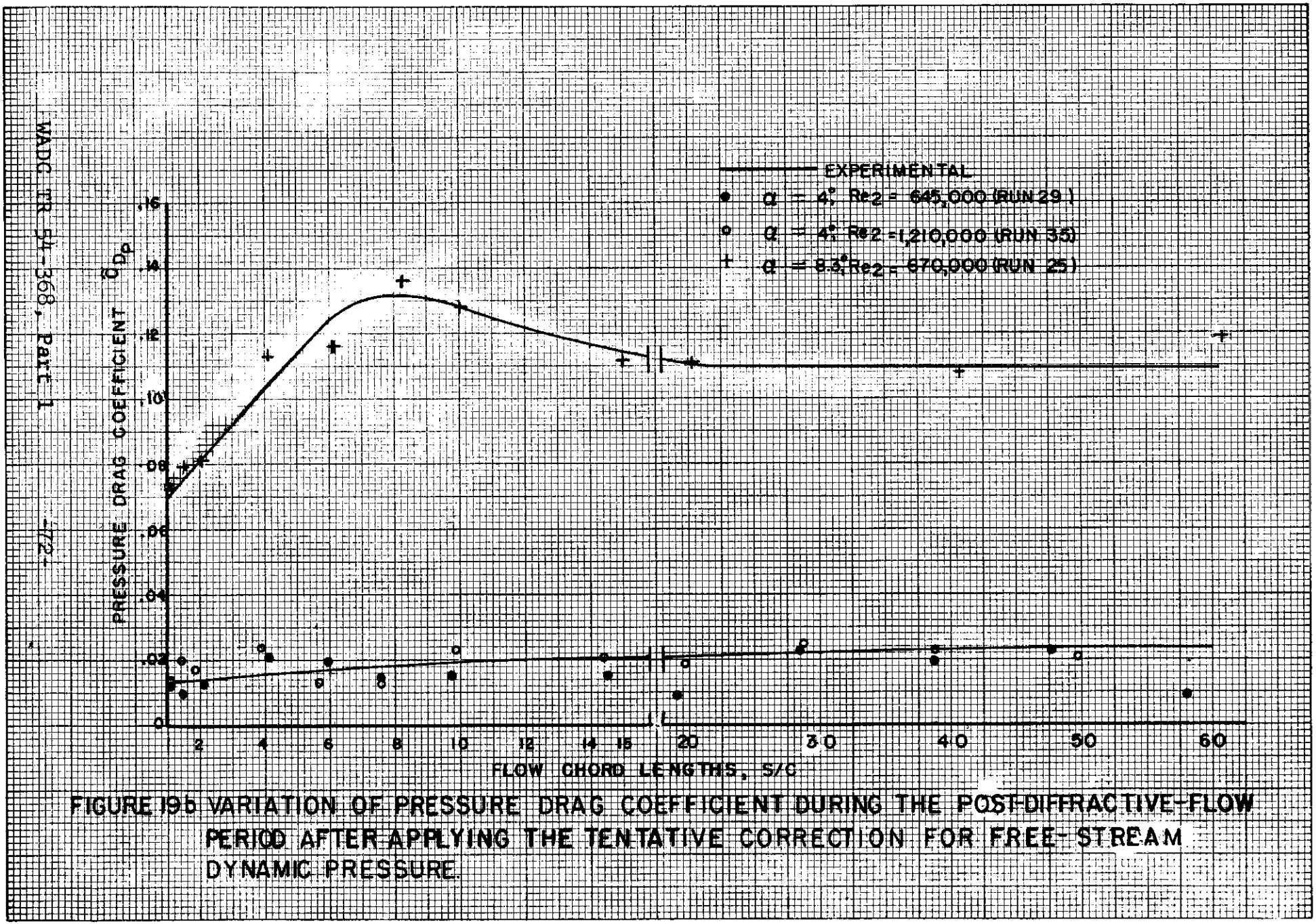

FIGURE 196 VARIATION OF PRESSURE DRAG COEFFICIENT DURING THE POST-DIFFRACTIVE-FLOW PERIOD AFTER APPLYING THE TENTATIVE CORRECTION FOR FREE-STREAM DYNAMIC PRESSURE.

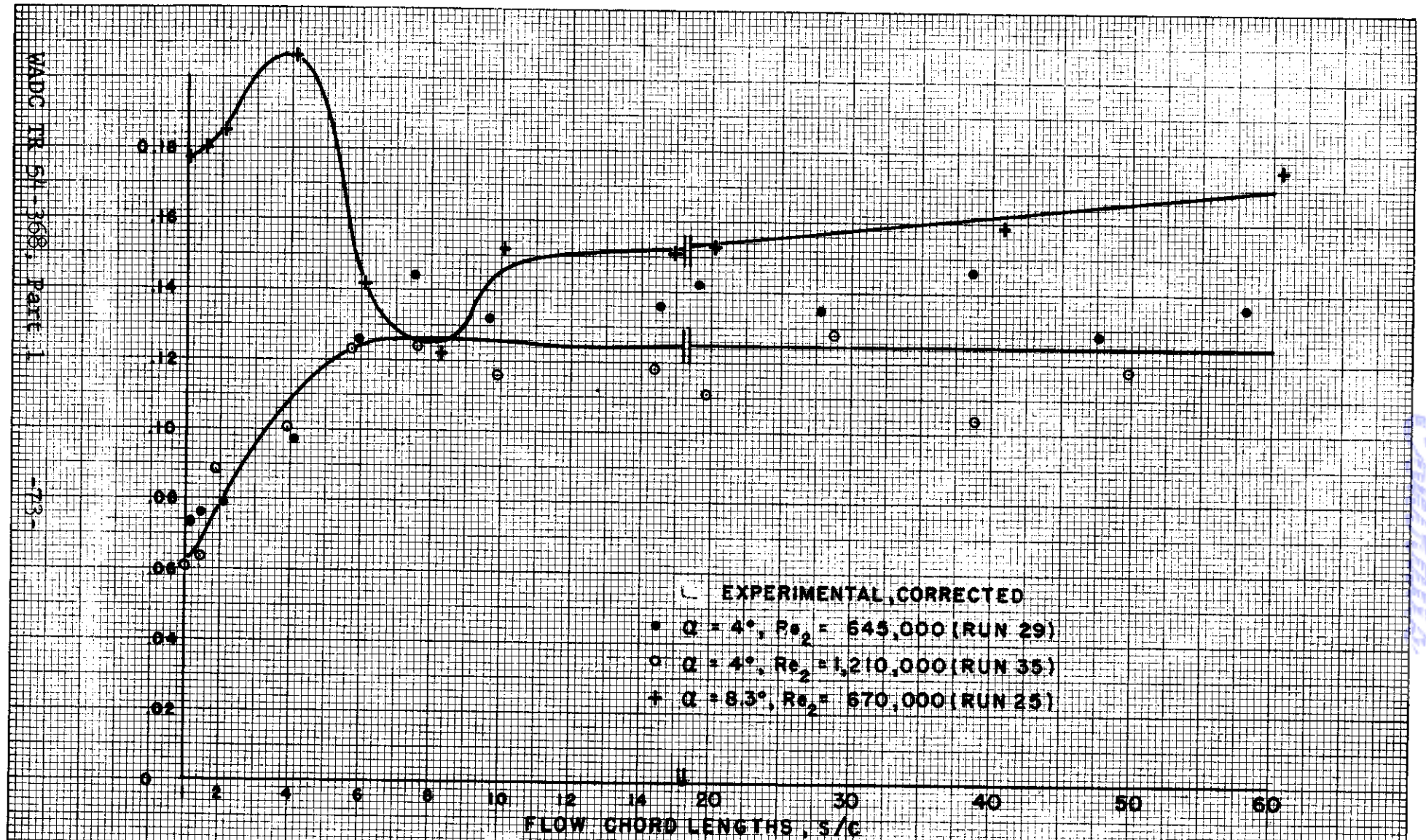

FIG. 19c VARIATION OF $C_{M_{c/2}}$ DURING THE POST-DIFFRACTIVE FLOW PERIOD, AFTER APPLYING THE TENTATIVE CORRECTION FOR FREE-STREAM DYNAMIC PRESSURE

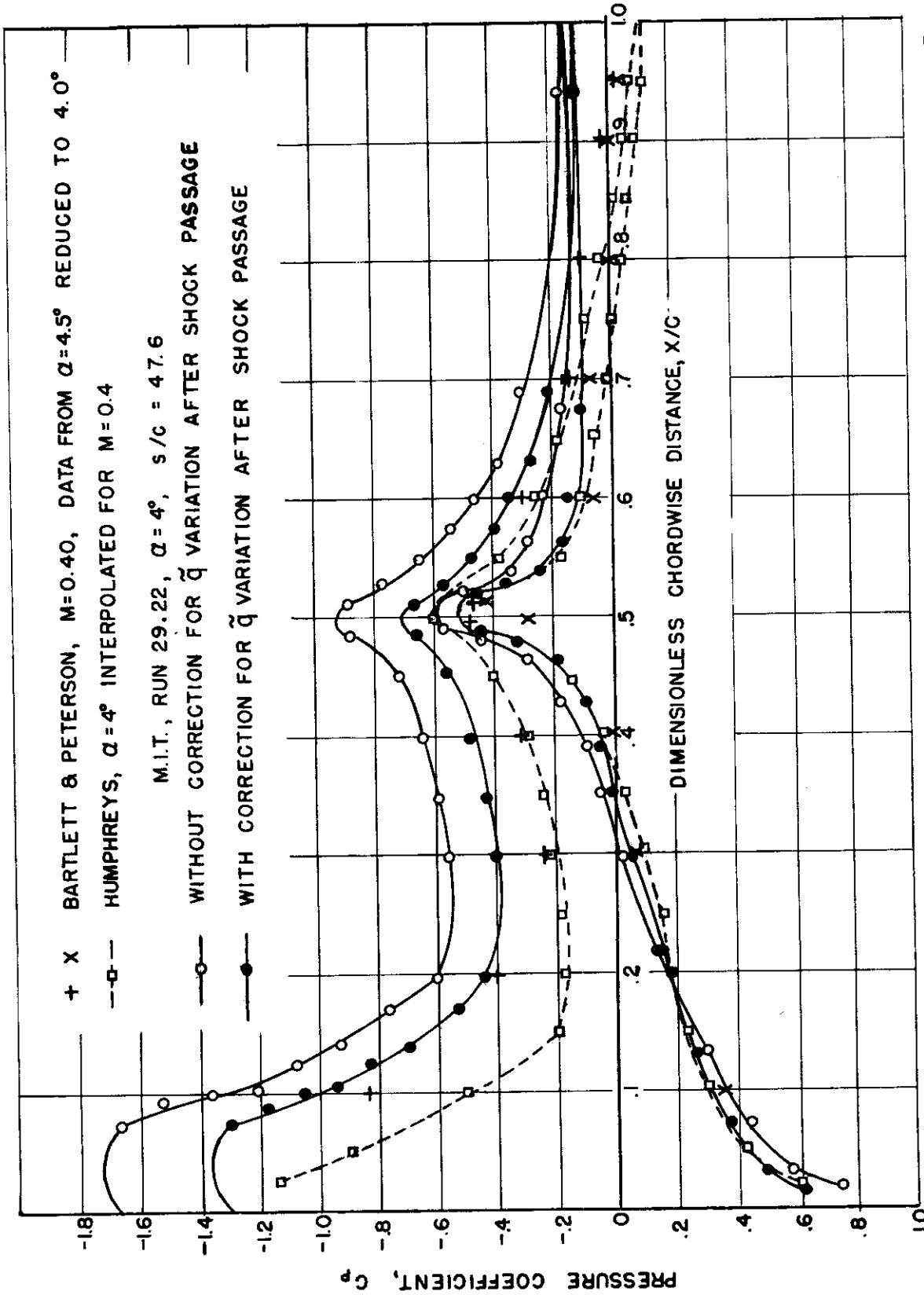

FIG. 20 COMPARISON OF STEADY-STATE PRESSURE DISTRIBUTIONS AROUND THE AIRFOIL FOR $\alpha = 4°$, $M = 0.4$

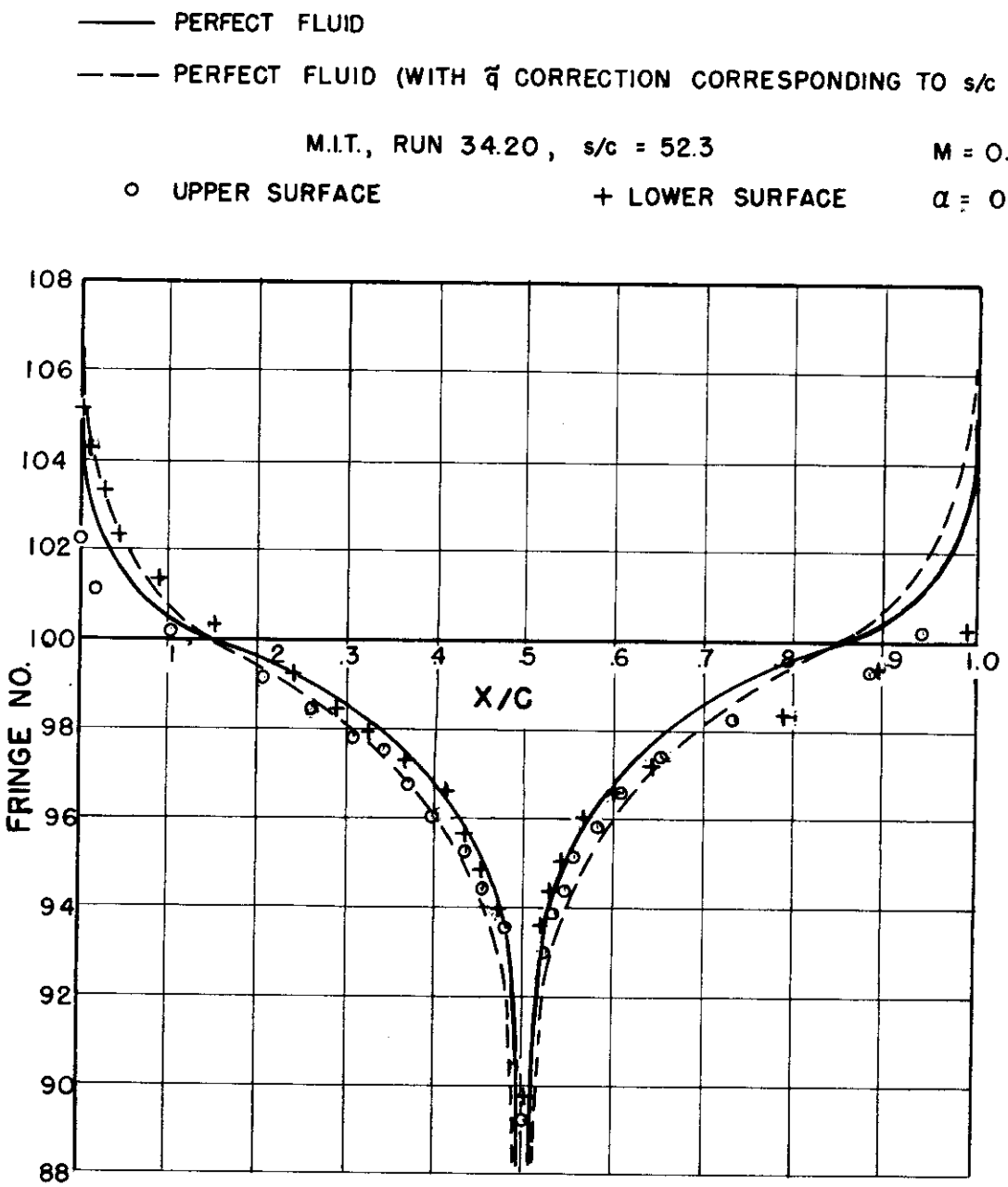

FIG.21 COMPARISON OF FRINGE DISTRIBUTION OVER THE SURFACE OF THE AIRFOIL ($\alpha = 0$, $M = 0.4$) WITH THEORETICAL RESULTS FOR NON-CONDUCTIVE INVISCID COMPRESSIBLE FLOW

TABLE 1

TEST CONDITIONS

Run Group	α	p_1	P_{21}	M_2	R_{e_2} x 10^{-6}
25	8.3	7.4 psia	1.81	.41	0.670
29	4	7.64 psia	1.78	.39	0.645
34	0	1 atm	1.77	.39	1.23
35	4	1 atm	1.77	.39	1.21